Ocean Engineering 365 (2026) 127083

Contents lists available at ScienceDirect

Ocean Engineering

journal homepage: www.elsevier.com/locate/oceaneng

Research paper

Sea-trial-validated frenet-frame MPC framework for formation control of multiple underactuated USVs under complex trajectories

Shunli Wang [a,b], Xiufen Ye [a,*], Shuxiang Guo [b,c,d], Chunying Li [b], Ronghao Zhang [a,b], Xihuan Hou [e]

[a] College of Intelligent Systems Science and Engineering, Harbin Engineering University, Harbin, 150001, China
[b] Advanced Institute for Ocean Research, Southern University of Science and Technology, Shenzhen, Guangdong, 518055, China
[c] Department of Electronic and Electrical Engineering, Southern University of Science and Technology, Shenzhen, Guangdong, 518055, China
[d] Aerospace Center Hospital, School of Life Science and the Key Laboratory of Convergence Medical Engineering System and Healthcare Technology, Ministry of Industry and Information Technology, Beijing Institute of Technology, Beijing, 100081, China
[e] School of Intelligence and Information Engineer, Tangshan University, Tangshan, Hebei, 063000, China

ARTICLE INFO

Keywords:
Unmanned surface vehicle swarm control
Frenet frame
Decoupled formation control
Reduced-order MPC

ABSTRACT

This paper presents a Frenet-frame-based formation control framework for multiple unmanned surface vehicles (USVs) to achieve cooperative trajectory tracking and formation keeping. To improve model accuracy, high-fidelity dynamic parameters of each USV are identified using sea-trial data collected from practical platforms, providing an accurate basis for model predictive control. To reduce the computational burden of coupled multi-degree-of-freedom MPC optimization, global position errors are decomposed in the Frenet coordinate framework, and a hierarchical error control mechanism is developed. The original coupled cooperative tracking problem is thereby transformed into a lightweight control problem. A shore-based centralized coordination architecture is adopted, where the ground station receives the states of all USVs and generates control commands, while the Mesh network serves only as the wireless communication infrastructure rather than an explicit inter-USV control topology. Real-sea formation experiments on a complex figure-eight trajectory are conducted, and a single-USV fault scenario is further tested. Results demonstrate that the proposed framework achieves effective trajectory tracking and formation keeping, while the single-USV propeller-failure test shows that the remaining USVs can continue the mission after one vehicle loses propulsion, providing a practical reference for multi-USV formation control applications.

1. Introduction

With the increasing demands for marine resource exploitation, maritime rights protection, and marine environmental monitoring, USVs have attracted extensive attention in the fields of ocean engineering and marine equipment in recent years because of their high maneuverability, flexible deployment, low operational cost, and reduced operational risk (Hung et al., 2023; Liu et al., 2021, 2025; Rui et al., 2026). As maritime mission areas continue to expand and mission types become increasingly complex, the limitations of single-USV systems in terms of spatial coverage, operational efficiency, and fault tolerance have become increasingly evident. Compared with single-USV platforms, multi-USV formation systems exhibit higher mission efficiency and stronger system redundancy, and have therefore become an important research direction in unmanned marine equipment (Liu et al., 2021; Suo et al., 2026; X. Zhou et al., 2025). For multi-USV systems, achieving trajectory tracking accuracy, formation-keeping stability, and control robustness under dynamic ocean disturbances is a key issue for practical engineering applications (Dong et al., 2025; Hung et al., 2023; Wang et al., 2024).

For underactuated USVs, since the sway degree of freedom cannot be directly actuated, trajectory tracking and formation control problems exhibit pronounced nonholonomic, nonlinear, and strongly coupled characteristics (Liao et al., 2015; Liu et al., 2017; Wu et al., 2025). In existing studies, path tracking is usually regarded as a fundamental problem in single-USV control, with the core issues lying in reference path generation and low-level control-law design (Hung et al., 2023). Under complex curved-path conditions, the Frenet/Serret–Frenet

* Corresponding author.
E-mail address: yexiufen@hrbeu.edu.cn (X. Ye).

https://doi.org/10.1016/j.oceaneng.2026.127083
Received 8 May 2026; Received in revised form 17 June 2026; Accepted 14 July 2026

coordinate framework can naturally decompose global position errors into tangential and normal components, thereby providing a clearer geometric interpretation for error modeling and controller design. It has thus become an important technical approach in path-tracking research (Han and Zhang, 2022; Li et al., 2023; Liao et al., 2015). Within this framework, many researchers have investigated motion control of USVs. Liao et al. established a path-tracking model for underactuated USVs based on Serret–Frenet coordinates and transformed the original coupled control problem into a more tractable form Liao et al. (2015). Han and Zhang further combined Frenet coordinates with model predictive control (MPC) to achieve trajectory generation, tracking optimization, and constraint handling under curved-path conditions (Han and Zhang, 2022). Meanwhile, line-of-sight (LOS), improved LOS, extended LOS (ELOS), and vector-field guidance methods have also been widely used to improve tracking performance under curved paths and disturbance environments (Fan et al., 2019; Liu et al., 2017; Wu et al., 2025). These studies indicate that the Frenet coordinate framework has clear advantages in representing complex path errors, reducing the difficulty of controller design, and supporting predictive control modeling (Han and Zhang, 2022; Li et al., 2023; Liao et al., 2015).

However, existing USV motion control studies based on the Frenet coordinate framework are still mainly focused on single-USV path tracking or trajectory control under idealized simulation conditions, while relatively limited attention has been paid to cooperative formation control of multiple underactuated USVs. In particular, in multi-USV systems, formation tracking requires not only handling the lateral and longitudinal errors of each USV relative to the reference path, but also further coordinating inter-USV relative positions, individual dynamic differences, and real-time control requirements under complex trajectories. Therefore, how to extend the Frenet coordinate framework from single-USV path tracking to cooperative formation control of multiple USVs, and how to combine it with practical platform dynamics and real-sea experimental validation to verify its engineering applicability, remain issues worthy of further investigation.

For cooperative formation control of multiple USVs, various control methods have been proposed. For example, Shi and Ye transformed the optimal formation problem of USVs into a Nash equilibrium seeking problem under a regularized game framework (Shi and Ye, 2024). Yu et al. further considered Stackelberg differential graphical game-based formation control under six-degree-of-freedom dynamics and input saturation constraints (Yu et al., 2024). Dong et al. proposed a sliding-mode control scheme for time-varying formation trajectory tracking by combining Frenet trajectory planning with an improved guidance strategy (Dong et al., 2025). Zhang et al. designed a dynamic sliding-mode fault-tolerant formation control method for actuator fault scenarios (Zhang et al., 2025). Recent studies have investigated multi-USV formation and cooperative tracking from different perspectives, including predefined-time/fixed-time convergence, reinforcement-learning-based coordination, tight formation control, and optimal trajectory tracking under disturbances (Song et al., 2025; Su et al., 2025; Suo et al., 2026; Wang et al., 2023, 2024; X. Zhou et al., 2025). More recent efforts have further extended formation control toward practical issues such as uncertainty compensation, obstacle avoidance, intermittent communication, fault tolerance, actuator saturation, collision avoidance, and safety-guaranteed optimization, including interval type-2 fuzzy formation-containment control, networked USV swarm control under communication constraints, fault-tolerant cooperative formation control for heterogeneous ships, and LMPC-based safety-enhanced distributed formation control for USVs (Chang et al., 2024, 2025; Lin et al., 2025; Sun et al., 2026; Zhang et al., 2026). These studies indicate that cooperative control of multiple USVs has evolved from basic trajectory tracking toward integrated problems involving formation keeping, uncertainty handling, obstacle avoidance, communication efficiency, constraint coordination, and reliable execution, thereby imposing higher requirements on predictive optimization, constraint handling, and real-time implementation.

In practical cooperative control systems, measurement limitations and actuator constraints can also significantly affect closed-loop performance. Recent studies on autonomous surface vessel platoon formation with limited field-of-view sensors and saturated actuators have shown that sensing restrictions and actuation limits should be explicitly considered in marine cooperative control (Naderolasli, 2026a). In addition, constrained nonlinear control studies on systems with limited sensing range or limited field-of-view sensors further indicate that measurement limitations, state constraints, and actuator saturation are common challenges in practical control systems (Naderolasli, 2026b, 2026c). These works suggest that practical USV formation control should move beyond ideal state-feedback assumptions and account for measurement imperfections, actuation limits, and real-time implementation constraints.

In this context, MPC has been widely applied to USV trajectory tracking and formation control because it can explicitly handle input constraints, state constraints, and trajectory errors within a receding-horizon optimization framework based on predictive models (Han and Zhang, 2022; Li et al., 2023; Yu et al., 2025; B. Zhou et al., 2025). For single-USV control, several studies have combined MPC with the Frenet/Serret–Frenet coordinate framework. For instance, Han and Zhang proposed a VSB-MPC method based on the Frenet framework to achieve path tracking and obstacle avoidance optimization under complex trajectories (Han and Zhang, 2022). Li et al. established a state-space model based on Serret–Frenet coordinates and introduced a risk-augmented term to improve single-USV trajectory tracking and obstacle avoidance performance (Li et al., 2023). However, such studies are mostly oriented toward single-USV motion control and have not fully considered cooperative errors and task consistency among multiple USVs in formation missions.

Although MPC has been widely used in USV trajectory tracking and formation control, its performance strongly depends on the accuracy of the prediction model. In many existing studies, the dynamic models used for MPC design are obtained from simulations, simplified assumptions, or idealized operating conditions. However, in real sea environments, hydrodynamic uncertainties, actuator saturation and rate constraints, external disturbances, and platform-to-platform dynamic differences may cause model mismatch, thereby degrading the prediction accuracy and closed-loop control performance of MPC. Therefore, for practical multi-USV formation control, it is necessary to identify control-oriented dynamic models based on real sea-trial data and verify whether the identified models can support reliable MPC implementation under actual marine conditions.

In addition, multi-USV formation control involves not only path-tracking accuracy but also formation-keeping constraints, inter-vehicle coordination, input limitations, and real-time computational efficiency. Directly applying full-state MPC to the whole formation may lead to a high-dimensional optimization problem, because the controller needs to simultaneously handle multi-vehicle states, formation geometry, path-following constraints, and actuator constraints. Liu et al. introduced MPC into multi-ship formation control under switching topologies and pointed out that increasing the prediction and control horizons leads to higher computational cost (Liu et al., 2021). Yu et al. further employed distributed MPC (DMPC) to address formation-keeping problems under communication constraints; however, distributed predictive control still relies on state information exchange among controllers, which may increase both communication and computational complexity (Yu et al., 2025). Zhou et al.'s study on event-triggered communication also indicates that limited bandwidth, communication delays, packet loss, and channel congestion may affect the engineering reliability of distributed multi-USV cooperation (B. Zhou et al., 2025). Moreover, most existing formation-control studies are still mainly validated in simulation environments, whereas real-sea experiments involving multiple USVs under complex trajectory tracking and fault conditions remain relatively limited. Therefore, how to reduce the optimization complexity while maintaining formation geometry and path-following performance, and how to validate the proposed framework through real-sea multi-USV experiments, remain important issues for practical applications.

In addition, from the perspective of validation methods, a large number of current studies on USV formation control are still mainly based on numerical simulations, while real-sea formation experiments involving multiple USVs under trajectory tracking and fault conditions remain relatively limited (Wu et al., 2024; Yu et al., 2025). Compared with single-USV path tracking or idealized cooperative scenarios, real marine environments introduce wind, wave, and current disturbances, state measurement errors, and uncertainties in actuator response. Multi-USV formation control not only faces problems such as model mismatch and state measurement errors, but also requires further evaluation of formation-keeping capability under complex trajectories and the influence of individual USV faults on overall cooperation. Therefore, it is necessary to examine the adaptability and robustness of the control architecture through fault-scenario tests. Conducting real-sea formation experiments of multiple underactuated USVs under complex trajectories and fault conditions is an important step for evaluating the engineering application value of cooperative control methods (Rui et al., 2026).

The main contributions of this paper can be summarized as follows. The main methodological novelty lies in reformulating the coupled multi-USV formation control problem into a reduced-order Frenet-frame-based control problem. By projecting the formation tracking errors into the Frenet frame, the proposed method decomposes the control objective into lateral path-convergence regulation and longitudinal formation-spacing coordination. Accordingly, MPC is only applied to the heading subsystem, while the longitudinal formation error is handled through speed coordination. This design differs from conventional full-state MPC formation control and single-USV Frenet-frame path tracking methods, because it reduces the online optimization dimension while retaining geometric error interpretability and constraint-handling capability. First, based on sea-trial data collected from practical USV platforms, the dynamic model parameters of each USV are identified separately, providing a model basis for the MPC controller that better reflects the motion characteristics of real platforms. Second, the Frenet coordinate framework is used to decompose the global formation tracking error into lateral and longitudinal components. On this basis, a hierarchical error-control mechanism is constructed, transforming the coupled multi-degree-of-freedom control problem into a lightweight cooperative control problem that combines heading predictive control with longitudinal speed coordination. Meanwhile, a shore-based centralized coordination architecture is adopted at the control-decision level, where the ground station uniformly performs state reception, formation-error calculation, and control-command generation. The Mesh self-organizing network serves only as the wireless communication infrastructure, rather than an explicit inter-USV control topology. Finally, real-sea multi-USV formation experiments involving a complex figure-eight trajectory and a simulated single-USV propeller-failure scenario are conducted to verify the practical performance of the proposed method in trajectory tracking, formation keeping, and mission continuation after one USV loses propulsion.

The remainder of this paper is organized as follows. Section 2 introduces the multi-USV experimental platform and the shore-based cooperative control architecture. Section 3 presents the USV modeling and model-parameter identification. Section 4 describes the MPC controller design based on the Frenet coordinate framework. Section 5 presents the real-sea experiments and result analysis. Section 6 concludes the paper.

2. System architecture of the Multi-USV platform

2.1. USV platform description

The USV is light and lightweight with a low-cost structure and favorable hydrodynamic performance. The hull is made of glass fiber reinforced polymer with buoyancy that is powerful, strong, stiff and corrosion resistant. It also reduces the overall weight.

Fig. 1 shows the 3D model of the platform. The lightweight hull reduces the hydrodynamical resistance and the onboard components (e.g., propulsion system, rudder and directional propeller, energy system, water pump unit, communication module, control system, and positioning and navigation) are compact.

The control system architecture of the USV is illustrated in Fig. 2, which mainly consists of the control unit, power unit, propulsion unit, navigation and positioning unit, and communication unit.

One of these components is the control unit, which acts as the main processing unit of the unmanned platform. It consists of the main control unit and the sensor unit and data processing unit. The main control component performs command processing and task scheduling, and the data processing module collects the platform state information. The data processing units produce multi-source sensor data fusion and processing to estimate the system state information and control feedback.

The power unit is provided by a battery pack in series and parallel connections and BMS, which provides stable power support of the electronic control system and the propulsion system of the platform. The propulsion unit uses two electric thrusters, as the primary motors and rudder plates are placed behind the thrusters. The latter ensures propulsion efficiency and improves turning performance and maneuverability. The navigation and positioning unit is composed by a high-precision BeiDou (BDS) positioning system and a navigation module. Multi-source information fusion is realized to provide reliable positioning and attitude information for the USV operation. The communication unit mainly uses a wireless data transmission radio, the 4G networks, BDS communication, and WiFi. By integrating multiple communication links, the reliability and flexibility of the communication system are improved, and it is possible to transmit and receive reliable data even in challenging sea environments.

2.2. Shore-based control architecture

To support coordinated operations in nearshore and offshore experimental scenarios, a shore-based control architecture for a USV swarm system is established, as shown in Fig. 3. The system adopts a hierarchical framework of “shore-based control–wireless communication–multi-USV execution,” in which the shore-based control center serves as the core unit. Based on the MATLAB platform, it performs task allocation, formation generation, path planning, and control command computation and transmission. In terms of multi-USV coordination, a centralized decision-making and distributed execution strategy is adopted, where the shore station is responsible for global task assignment and formation planning, while each USV independently executes trajectory tracking and motion control according to the

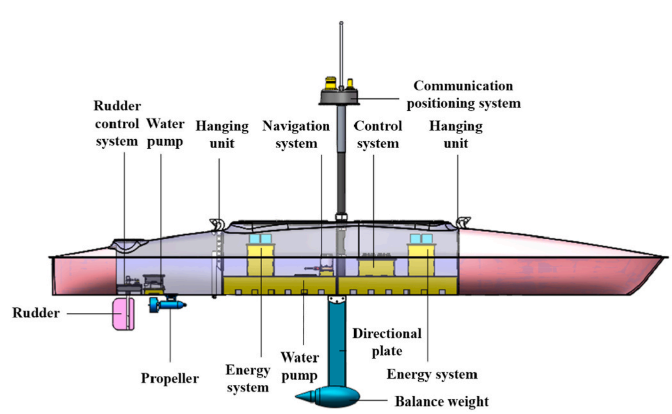

Fig. 1. The structure of the Unmanned Surface Vehicle.

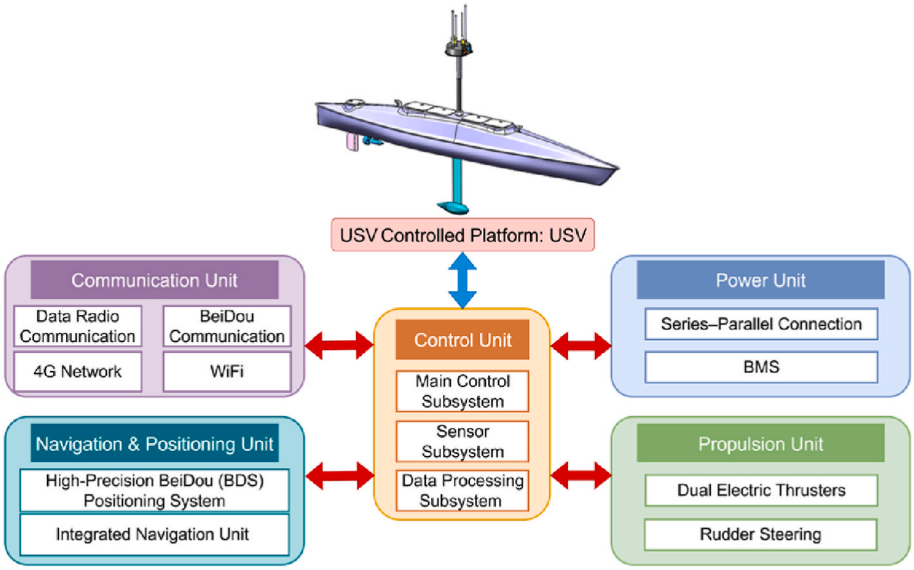

Fig. 2. The block diagram of the control system.

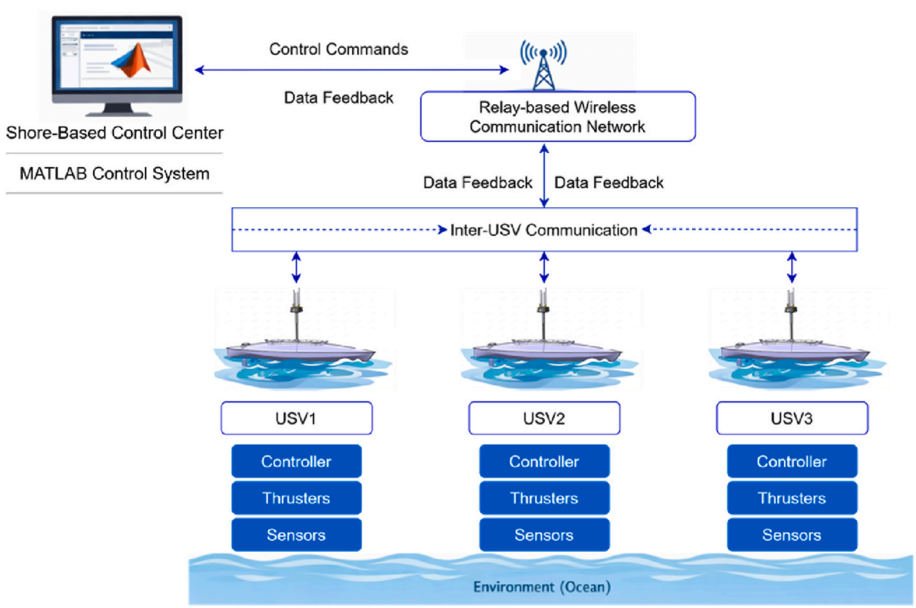

Fig. 3. System architecture of the Multi-USV platform.

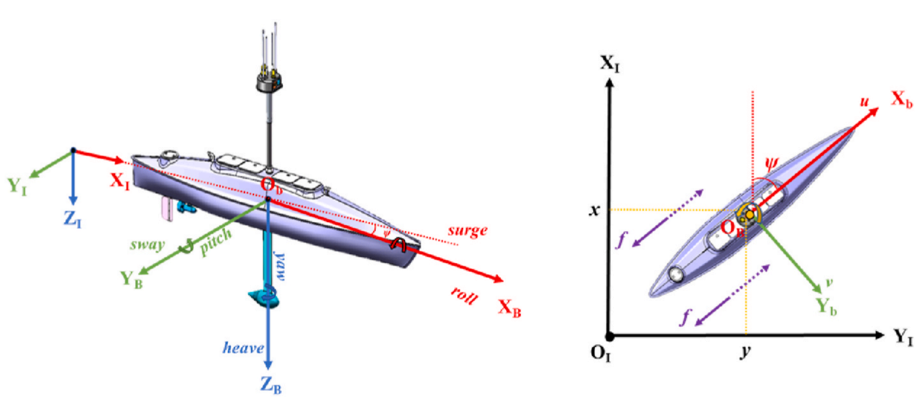

Fig. 4. Coordinate setup: The inertia coordinate is $O_IX_IY_IZ_I$, and the robot body coordinate is $O_bX_bY_bZ_b$. Translation and rotational movements are specified along each axis.

received commands, thereby enabling coordinated multi-vehicle operations (see Fig. 4).

At the communication level, a Mesh self-organizing network is used as the wireless transmission infrastructure to improve link robustness in complex marine environments. It should be noted that this Mesh network does not define the cooperative control topology. In the proposed architecture, each USV sends its own navigation states to the shore station, and the shore station computes and returns the corresponding control commands. Thus, the system adopts centralized decision making and distributed onboard execution over a mesh-based communication backbone.

3. USV modeling and system identification

3.1. Kinematic model of the USV

Before establishing the USV dynamic model, the reference coordinate systems are defined. Typically, two frames are used: an inertial (earth-fixed) frame and a body-fixed frame. Since different state variables are defined in different frames, coordinate transformations between these frames must be performed through rotation matrices or homogeneous transformation matrices. Such coordinate transformations constitute a fundamental step in the modeling and control analysis of USVs.

The kinematic model of a USV describes the geometric relationship between the rate of change of position and orientation and the velocity components of the vehicle. This model reflects only the rigid-body motion in space and does not involve parameters such as mass, inertia, or external hydrodynamic forces. Therefore, it characterizes the mathematical relationship among the vehicle's position, linear velocity, and angular velocity purely from a geometric perspective.

The pose vector of the USV in the inertial frame is defined as

$$\eta_1 = [x, y, z]^T, \eta_2 = [\phi, \theta, \psi]^T \tag{1}$$

where x, y, z denote the position coordinates, and ϕ, θ, ψ represent the roll, pitch, and yaw angles, respectively.

In the body-fixed frame, the velocity vector of the USV can be expressed as

$$\nu_1 = [u, v, w]^T, \nu_2 = [p, q, r]^T \tag{2}$$

where u,v,w are the surge, sway, and heave velocities, and p,q,r denote the angular velocities about the body-fixed axes. The resultant forces and moments acting on the vehicle are defined as

$$\tau_1 = [X, Y, Z]^T, \tau_2 = [K, M, N]^T \tag{3}$$

The body-fixed frame is attached to the USV, with the $\boldsymbol{x}_b$-axis pointing forward along the hull, the $\boldsymbol{y}_b$-axis pointing laterally, and the $\boldsymbol{z}_b$-axis completing the right-handed coordinate system. The variables u, v, w denote the translational velocities along these body-fixed axes, while p, q, r denote the corresponding angular velocities.

The transformation relationship of the state variables between the inertial frame and the body-fixed frame can be written as

$$\dot{\eta}_1 = R(\eta_2)\nu_1 \tag{4}$$

$$\dot{\eta}_2 = T(\eta_2)\nu_2 \tag{5}$$

where $R(\eta_2)$ is the rotation matrix (direction cosine matrix) determined by the Euler angles, which transforms the linear velocity from the body-fixed frame to the inertial frame, and $T(\eta_2)$ is the attitude transformation matrix describing the relationship between the angular velocity vector and the Euler angle rates. Accordingly, the complete kinematic relationship can be written in a compact form as

$$\widehat{n} = J(\eta)\nu \tag{6}$$

where

$$\eta = \left[\eta_1^T, \eta_2^T\right]^T, \nu = \left[\nu_1^T, \nu_2^T\right]^T \tag{7}$$

and

$$J(\eta) = \begin{bmatrix} R(\eta_2) & 0 \\ 0 & T(\eta_2) \end{bmatrix} \tag{8}$$

The matrices $R(\eta_2)$ and $T(\eta_2)$ form the velocity map from body frame to inertial frame that allows us to translate velocity variables from bodyframe to position and attitude rates from inertial frames, which serves as the basis for dynamic modeling and controller design of USV systems.

3.2. Dynamic modeling

The USV is mainly subjected to thrust, hydrodynamic effects, and restoring forces due to gravity and buoyancy. In this study, the vehicle dynamics are modeled using the Newton–Euler formulation. According to the modeling framework proposed by Fossen (Källström, 1996), the USV can be regarded as a rigid body with constant mass and inertia. Considering the planar motion of the vehicle, The 3-DOF dynamics in surge, sway, and yaw can be written as

$$M\dot{v} + C(v)v + D(v)v + g(\eta) = \tau \tag{9}$$

where M denotes the inertia matrix including the added mass; $C(\nu)$ represents the Coriolis and centripetal matrix; $D(\nu)$ is the hydrodynamic damping matrix; and $\boldsymbol{\tau}$ denotes the generalized control input vector, which includes the propulsion forces and moments acting on the USV as well as possible environmental disturbances.

By combining the kinematic and dynamic formulations and neglecting the coupling among degrees of freedom, the USV model can be expressed as in Eq. (10).

$$\begin{cases} \dot{x} = u\cos\psi - v\sin\psi \\ \dot{y} = u\sin\psi - v\cos\psi \\ \dot{\psi} = \dot{r} \\ m_u\dot{u} + c_u u + d_u u|u| + g_u = \tau_u \\ m_v v + c_v v + d_v v|v| + g_v = \tau_v \\ m_r\dot{r} + c_r r + d_r r|r| + g_r = \tau_r \end{cases} \tag{10}$$

where m_i, c_i, and d_i denote the equivalent inertia, linear damping, and nonlinear damping coefficients, respectively, and g_i represents the constant bias or slowly varying unmodeled term in each motion channel.

To enable tractable controller design, the full model was reduced to Eq. (11). Under the Frenet-frame formulation, the system is naturally decoupled into lateral and longitudinal dynamics. Hence, intermediate coupling terms and higher-order dynamics are neglected, as they are either implicitly embedded in the error dynamics or compensated by the MPC–PID control structure. This reduction preserves the essential control-relevant dynamics without compromising stability or tracking performance.

$$\begin{cases} \dot{\psi} = \dot{r} \\ m_u\dot{u} + c_u u + d_u u|u| + g_u = \tau_u \\ m_r\dot{r} + c_r r + d_r r|r| + g_r = \tau_r \end{cases} \tag{11}$$

where $\dot{\psi}$ denotes the yaw angle, u is the surge velocity, and r is the yaw rate. τ_u and τ_r represent the control force in the surge direction and the control moment in the yaw direction, respectively.

m_u and m_r denote the equivalent inertia coefficients, c_u and c_r denote the linear damping coefficients, d_u) and d_r denote the nonlinear damping coefficients, and g_u and g_r represent constant bias terms or slowly varying unmodeled effects in the corresponding motion channels. In this reduced model, the sway dynamics are not explicitly retained; instead, the lateral tracking behavior is regulated through the yaw angle and yaw rate under the Frenet-frame error formulation.

3.3. Parameter identification for MPC model

Accurate mathematical modeling of an underwater vehicle often relies on system parameter identification techniques. Various algorithms have been used for dynamic parameter identification in practice, such as maximum likelihood estimation, least squares methods, Kalman filtering, and neural networks. The vehicle's dynamic model is nonlinear in structure, but its parameters appear linearly within the coefficients. In this work, we adopt the least squares method for parameter identification, mainly because of its good consistency, robustness, and strong fitting ability—especially when dealing with noisy measurement data. This approach has also been widely adopted in previous studies and has demonstrated satisfactory identification accuracy (Huang et al., 2020).

Prior to parameter identification, dedicated experiments are conducted to collect the required motion and control data. A linear constant-speed experiment is performed to obtain the relationship between the USV surge velocity and thrust, while an in-situ circular motion experiment is carried out to acquire the angular velocity and torque data of the USV. Experimental measurements are used to estimate the unknown parameters via the identification scheme described below.

Assume that the system model to be identified is given as:

$$y_0(t) = H(x(t), t, \theta) \tag{12}$$

where t denotes time, $y_0(t) \in \mathbb{R}^{n\times 1}$ represents the observation vector, $x(t) \in \mathbb{R}^{m\times 1}$ denotes the time-varying regressor vector, and $\theta \in \mathbb{R}^{p\times 1}$ is the parameter vector to be estimated. According to the least-squares estimation, the expression of the parameter $\widehat{\theta}_{LS}$ can be obtained as:

$$\widehat{\theta}_{LS} = \left(H^T H\right)^{-1} H^T y \tag{13}$$

Taking the yaw degree of freedom as an example, let $\theta = [m_r \quad c_r \quad d_r \quad g]$ denote the parameter vector to be identified, τ_r denote the yaw moment obtained from the sea trials, $\dot{\nu}$ and ν denote the yaw angular acceleration and yaw rate, respectively, and n denote the total number of measured data points. Then, the identification problem can be expressed in the following form:

$$\begin{bmatrix} \tau_{r,1} \\ \vdots \\ \tau_{r,k} \\ \vdots \\ \tau_{r,n} \end{bmatrix} = \begin{bmatrix} \dot{\nu}_{r,1} & \nu_{r,1} & \nu_{r,1}|\nu_{r,1}| & 1 \\ \vdots & \vdots & \vdots & \\ \dot{\nu}_{r,k} & \nu_{r,k} & \nu_{r,k}|\nu_{r,k}| & 1 \\ \vdots & \vdots & \vdots & \\ \dot{\nu}_{r,n} & \nu_{r,n} & \nu_{r,n}|\nu_{r,n}| & 1 \end{bmatrix} \begin{bmatrix} m_r \\ c_r \\ d_r \\ g \end{bmatrix} \tag{14}$$

The matrix in the above equation can be further expressed as:

$$H = \begin{bmatrix} \dot{\nu}_{r,1} & \nu_{r,1} & \nu_{r,1}|\nu_{r,1}| & 1 \\ \vdots & \vdots & \vdots & \\ \dot{\nu}_{r,k} & \nu_{r,k} & \nu_{r,k}|\nu_{r,k}| & 1 \\ \vdots & \vdots & \vdots & \\ \dot{\nu}_{r,n} & \nu_{r,n} & \nu_{r,n}|\nu_{r,n}| & 1 \end{bmatrix}, y(t) = \left[\tau_{r,1} \cdots \tau_{r,k} \cdots \tau_{r,n}\right]^T \tag{15}$$

Then, the least-squares method can be used to calculate the parameter vector θ according to Eq. (13), thereby identifying the yaw-degree-of-freedom model. The surge-degree-of-freedom model can be identified in the same manner.

4. Formation control algorithm

To achieve stable formation control of multiple USVs under complex path conditions, a decoupled control approach within the Frenet coordinate framework is developed. Different from the traditional control strategy based on Euclidean distance error, this paper first maps the global position error to the path-related local coordinate system, thus decomposing the error into horizontal error and vertical error with clear physical significance.

On this basis, a unified decoupling control framework is constructed: lateral error is used for course adjustment and longitudinal error is used for speed adjustment, which fundamentally avoids the control conflict caused by the coupling of direction and speed.

Furthermore, to enhance control efficiency and real-time performance, MPC is applied only to the heading subsystem, converting the original full-state optimization problem into a reduced-order subsystem formulation. While preserving control performance, this approach effectively lowers computational complexity and improves system stability and practical feasibility under complex trajectories.

4.1. Formation error modeling and coordination strategy

4.1.1. Error modeling in Frenet coordinate frame

To accurately characterize the tracking error of a USV formation system, an error modeling approach within the Frenet coordinate framework is adopted. This method transforms the position error from the global coordinate system into a path-aligned local coordinate frame, thereby achieving effective decoupling between lateral and longitudinal errors.

Within the virtual structure-based formation framework, the desired positions of follower USVs are generated relative to a central guiding point. Let the central guiding point be denoted as $\mathbf{p}_o = [x_o, y_o]^T$, and the relative position of the k-th follower in the formation (ρ, θ) be represented in polar coordinates. Then, the corresponding desired guiding point can be expressed as:

$$\mathbf{P}_{fk} = \mathbf{p}_0 + R(\phi_0) \begin{bmatrix} \rho \cos\theta \\ \rho \sin\theta \end{bmatrix} \tag{16}$$

where ϕ_o denotes the heading angle of the central guiding point, and $R(\phi_o)$ is the rotation matrix given by:

$$R(\phi_0) = \begin{bmatrix} \cos\phi_0 & -\sin\phi_0 \\ \sin\phi_0 & \cos\phi_0 \end{bmatrix} \tag{17}$$

This transformation maps the formation configuration from the Body-fixed coordinate system to the Earth-fixed coordinate system.

Let the actual position of the k-th USV be $\mathbf{p}_k = [x_k, y_k]^T$, and its corresponding desired guiding point be $\mathbf{p}_{fk} = [x_k^d, y_k^d]^T$. The position tracking error in the global coordinate system is defined as:

$$\begin{cases} e_{xk} = x_{kl}^d - x_k \\ e_{yk} = y_{kl}^d - y_k \end{cases} \tag{18}$$

Although this definition is intuitive, it does not distinguish between errors along and perpendicular to the reference path. To address this limitation, the error is further projected into the Frenet coordinate frame associated with the reference trajectory.

Let ψ_d denote the tangential direction angle of the reference path. A rotation matrix is constructed as:

$$R(\psi_d) = \begin{bmatrix} \cos\psi_d & -\sin\psi_d \\ \sin\psi_d & \cos\psi_d \end{bmatrix} \tag{19}$$

Then, the error expressed in the Frenet coordinate frame can be written as:

$$\begin{bmatrix} e_y \\ e_x \end{bmatrix} = R(\psi_d) \begin{bmatrix} x_k^d - x_k \\ y_k^d - y_k \end{bmatrix} \tag{20}$$

where e_y represents the lateral error, i.e., the deviation perpendicular to the path. e_x represents the longitudinal error, i.e., the deviation along the path direction.

This transformation essentially projects the global position error onto the tangential and normal directions of the reference trajectory. Compared with conventional Euclidean distance-based error formulations, the proposed representation provides clearer physical interpretation and facilitates control decoupling.

Specifically, the lateral error e_y mainly affects heading control and is used to ensure path convergence, while the longitudinal error e_x governs velocity regulation and is used to maintain formation spacing.

In this study, the path tangential angle ψ_d is approximated using the heading angle of a virtual guiding point, so that the path curvature does not need to be computed explicitly. This simplification reduces the computational load and makes real-time implementation more practical for multi-USV systems.

Compared with conventional Euclidean distance-based error definitions, the proposed approach separates the error into lateral and longitudinal components. These components have clearer physical meanings and are more convenient for subsequent decoupled control design.

4.1.2. Decoupled formation control with longitudinal coordination

A decoupled formation control strategy is constructed from the error representation in the Frenet coordinate frame. In this framework, lateral and longitudinal errors are handled separately through heading and speed control. This separation avoids the coupling between direction and velocity that is often observed in Euclidean distance-based methods, which helps improve convergence behavior and overall system stability.

Specifically, the lateral error e_y is used for heading adjustment to achieve path-following, while the longitudinal error e_x is used to regulate the speed for maintaining formation spacing. To reduce the accumulation of longitudinal errors during maneuvers, a coordination mechanism based on local error feedback is further introduced. This mechanism allows cooperative behavior to emerge without relying on an explicit communication topology.

(1) Lateral Error Regulation

The lateral error e_y describes the deviation of the USV from the reference path in the normal direction. When $e_y \neq 0$, the desired heading angle is adjusted to guide the USV toward the path, thereby ensuring stable trajectory tracking. To enhance the dynamic performance and constraint-handling capability of the heading control, a MPC scheme is adopted for lateral error regulation. The detailed design of the MPC controller will be presented in Section 4.2.

Since the lateral error exclusively affects heading control, the proposed approach effectively avoids interference from longitudinal dynamics, reduces system oscillations, and improves robustness and stability under complex trajectory conditions.

(2) Longitudinal Error Regulation and Coordination Mechanism

The longitudinal error e_x represents the deviation along the path direction and directly influences the relative spacing among formation members. To regulate this error, a longitudinal coordination mechanism based on error feedback is designed, where the desired speed is defined as:

$$u_i = \lambda \cdot e_x \cdot u_{ref} \tag{21}$$

where u_{ref} is the desired cruising speed, $\lambda > 0$ is the longitudinal gain, e_x is the longitudinal error.

This mechanism exhibits the following properties:

- When $e_x > 0$ (the USV lags behind), the speed is increased to accelerate convergence
- When $e_x < 0$ (the USV moves ahead), the speed is reduced to restore the desired spacing

Compared with conventional consensus-based methods, the proposed approach does not rely on explicit communication topology or neighbor information exchange. Instead, coordination is achieved through local error feedback, enabling implicit cooperation among formation members while significantly reducing system complexity.

In summary, the proposed decoupled control strategy combined with the longitudinal coordination mechanism improves convergence speed, stability, and scalability of the multi-USV formation system, while maintaining a simple and efficient control structure. This study transforms the path-following problem into two mutually independent control subproblems—lateral and longitudinal—thereby avoiding the control conflicts caused by the coupling between heading and speed in conventional methods.

4.2. MPC-based heading control design

Unlike the indirect coupling between error and control input in conventional approaches, this study explicitly incorporates the lateral error into the heading control loop and performs optimization within a MPC framework, thereby enhancing system stability and convergence performance under complex path conditions. Based on the error modeling and decoupled control framework established in Section 4.1, the heading control problem is formulated independently, and MPC is employed for optimization. It is worth noting that, in contrast to traditional implementations where MPC is applied to full-state or position tracking, this work constructs the predictive model exclusively for the heading subsystem, thereby enabling a reduced-order optimization control strategy.

4.2.1. Heading reference generation based on lateral error

In the Frenet frame, the lateral error e_y represents the deviation of the USV from the reference path in the normal direction. To achieve path convergence, the desired heading angle is constructed based on the lateral error. Let the tangential direction angle of the reference path be ψ_d, then the desired heading is defined as:

$$\psi_{ref} = \psi_d + \Delta\psi \tag{22}$$

where the heading correction term $\Delta\psi$ is generated from the lateral error as

$$\Delta\psi = \arctan\left(k_y e_y\right) \tag{23}$$

where $k_y > 0$ is the lateral error gain.

In the proposed method, the lateral error is converted into a heading correction through a nonlinear mapping. This mapping produces smooth adjustments when the error is small and increases the correction as the error becomes larger, which helps improve stability while maintaining convergence speed. Compared with look-ahead-based guidance methods, this approach does not require additional waypoint selection, leading to a simpler structure and better adaptability. In addition, the heading reference is generated directly from the lateral error, so the control objective is expressed in terms of error feedback rather than geometric path tracking, which is consistent with the decoupled control framework.

4.2.2. Linearized state-space prediction model of USV

To design the heading controller, a state-space model of the USV is established. Considering planar motion, the nonlinear dynamics can be expressed as:

$$\dot{x} = f(x, \tau) \tag{24}$$

The state vector x and control input τ are defined as $x = [u, v, \psi, r]^T$, $\tau = [\tau_u, \tau_r]^T$, in this equation, u, v denote surge and sway velocities, ψ is the heading angle, r is the yaw rate, τ_u is thrust, and τ_r is yaw moment. The system dynamics are given by:

$$\dot{x} = \begin{bmatrix} R(\psi)v \\ M^{-1}(\tau - D(v))v \end{bmatrix} \tag{25}$$

where M and $D(v)$ denote the inertia and damping matrices:

$$M = \begin{pmatrix} m_u & 0 & 0 \\ 0 & m_v & 0 \\ 0 & 0 & m_r \end{pmatrix} \tag{26}$$

$$D = \begin{pmatrix} c_u + d_u|u| & 0 & 0 \\ 0 & c_v + d_v|v| & 0 \\ 0 & 0 & c_r + d_r|r| \end{pmatrix} \tag{27}$$

(1) Linearized error model

The nonlinear system is linearized around a reference state (x_d, τ_d) using first-order Taylor expansion:

$$\dot{\widetilde{x}} = A\widetilde{x} + B\widetilde{\tau} \tag{28}$$

where $\widetilde{x} = x - x_d, \widetilde{\tau} = \tau - \tau_d, A = \left.\frac{\partial f(x,\tau)}{\partial x}\right|_{x=x_d,\tau=\tau_d}, B = \left.\frac{\partial f(x,\tau)}{\partial \tau}\right|_{x=x_d,\tau=\tau_d}$

(2) Discretization

The continuous model is discretized with sampling time T_s:

$$\widetilde{x}(k+1) = A_d\widetilde{x}(k) + B_d\widetilde{\tau}(k) \tag{29}$$

where $A_d = I + T_S A, B_d = T_S B$, I is the identity matrix,and T_s is the sampling period.

(3) Model reduction under decoupled control

According to the decoupling strategy in Section 4.1, surge velocity and heading are controlled independently. The surge velocity is regulated by a PID controller, while heading is optimized via MPC. Therefore, thrust can be treated as a known input and excluded from the MPC decision variables. The system is thus reduced to a heading-related subsystem:

$$x_\psi = [\psi, r]^T, \tau_\psi = \tau_r \tag{30}$$

where $\boldsymbol{x}_\psi$ is the heading-related state vector, ψ denotes the yaw angle, $\boldsymbol{\tau}_\psi$ is the control input of the heading subsystem, and $\boldsymbol{\tau}_r$ represents the yaw control moment.

The corresponding discrete-time prediction model is given by:

$$\widetilde{x}_\psi(k+1) = A_\psi\widetilde{x}_\psi(k) + B_\psi\widetilde{\tau}_\psi(k) \tag{31}$$

This reduction eliminates coupling effects and significantly decreases computational complexity while preserving control performance.

4.2.3. Optimization objective design for heading tracking

To achieve effective tracking of the desired state, an appropriate optimization objective must be constructed. Meanwhile, from an energy-efficiency perspective, the control input magnitude should be minimized as much as possible. To prevent infeasibility of the optimization problem, a slack variable is introduced into the cost function for regulation. Based on the aforementioned heading subsystem prediction model, the optimization objective for heading tracking is formulated as:

$$J(k) = \sum_{j=1}^{N_p-1} \widetilde{x}_\psi^T(k+j)Q\widetilde{x}_\psi(k+j) + \sum_{j=1}^{N_c} \widetilde{\tau}_\psi{}^T(k+j-1)R\widetilde{\tau}_\psi(k+j-1) + \widetilde{x}^T(k+N_p)P\widetilde{x}(k+N_p) + \rho\varepsilon^2 \tag{32}$$

where N_p andN_c are prediction and control horizons, Q, R are the state weighting matrix and control weighting matrix, respectively. ρ denotes the weighting coefficient, and ε is the slack variable.

Based on the discrete-time prediction model in Eq. (31), the predicted heading-related states are stacked and expressed as a linear function of the current state and the future yaw-moment input sequence. Since the MPC cost function is quadratic in the predicted states and control inputs, it can be reformulated as a standard constrained QP with respect to the stacked control vector.

(1) Error-driven heading tracking

Unlike conventional geometric tracking, the heading reference is driven by the lateral error e_y.

Therefore, the optimization objective can be equivalently expressed as:

$$min(\psi - \psi_d(e_y)) \rightarrow 0 \tag{33}$$

That is:

$$\begin{aligned} &\underset{\widetilde{\tau}^*}{\operatorname{argmin}} \mathbf{J}(k) \\ &s.t. \\ &\widetilde{\mathbf{x}}(k+j+1) = \widetilde{\mathbf{A}}\widetilde{\mathbf{x}}(k+j) + \widetilde{\mathbf{B}}\widetilde{\tau}(k+j), j = 0, 1\cdots, N_p - 1 \\ &\widetilde{\tau}(k+j) = \widetilde{\tau}(k+j-1), j \geq N_c + 1 \\ &\widetilde{\tau}_{\min} \leq \widetilde{\tau} \leq \widetilde{\tau}_{\max} \end{aligned} \tag{34}$$

where $\widetilde{\tau}_{\max}$ and $\widetilde{\tau}_{\min}$ are the limit value of the control input. $\widetilde{\tau}*$ denotes the optimal control input sequence, $\mathbf{J}(k)$ is the objective function at the current sampling instant k, $\widetilde{X}(k+j)$ is the predicted heading-related state at the j-th prediction step, and $\widetilde{\tau}(k+j)$ is the corresponding predicted control input. $\widetilde{A}$ and $\widetilde{B}$ are the discrete-time prediction matrices. $\boldsymbol{N}_p$ and Nc denote the prediction horizon and the control horizon, respectively.

This design drives heading regulation based on the lateral error, avoiding the coupling effects and control conflicts introduced by global position errors, while maintaining consistency with the proposed decoupled control structure. Compared with conventional position-tracking-based optimization strategies, the control objective is reformulated as error-driven heading regulation, thereby further enhancing the effectiveness and consistency of the decoupled control framework.

(2) Constraint condition

Considering the physical limitations of the actual system, control constraints are introduced:

$$\tau_{\min} \leq \tau_r(k) \leq \tau_{\max} \tag{35}$$

To enhance input smoothness and system stability, a control increment constraint is introduced:

$$\Delta\tau_{\min} \leq \Delta\tau_r(k) \leq \Delta\tau_{\max} \tag{36}$$

4.2.4. Solution procedure of the control algorithm

The above finite-horizon optimization problem can be converted into a standard constrained quadratic programming problem (QP). The decision variable is the stacked yaw-moment input vector over the control horizon. The Hessian matrix in the quadratic cost is determined by the lifted prediction matrix and the block-diagonal state and input weighting matrices, while the gradient vector is determined by the current prediction error between the predicted heading-state sequence and the reference sequence. Therefore, the QP problem can be written in the standard form:

$$\begin{aligned} &\min_U \mathbf{J}(k) = \left[\mathbf{U}(k)^T, \varepsilon\right]\mathbf{H}(k)\left[\mathbf{U}(k)^T, \varepsilon\right]^T + \mathbf{G}(k)\left[\mathbf{U}(k)^T, \varepsilon\right]^T \\ &\text{s.t. } \mathbf{U}_{\min} \leq \mathbf{U}(k) \leq \mathbf{U}_{\max} \end{aligned} \tag{37}$$

where $\mathbf{U}_k = (\tau(k), \tau(k+1)\cdots\cdots\cdots\tau(k+N_c-1))^T$, $\mathrm{H(k)} = \begin{bmatrix} \Theta^T Q\Theta + R & 0 \\ 0 & \rho \end{bmatrix}$, $\mathrm{G(k)} = \begin{bmatrix} 2\boldsymbol{e}_k^T Q\Theta & 0 \end{bmatrix}$, $\boldsymbol{e_k} = \Phi\widetilde{\mathbf{x}}(k)$.

The matrix Θ in the definition of H, and the matrix Φ in the definition of G are expressed as follows:

$$\Theta = \begin{bmatrix} \mathbf{B} & \mathbf{0} & \mathbf{0} & \mathbf{0} \\ \mathbf{AB} & \mathbf{B} & \mathbf{0} & \mathbf{0} \\ \cdots & \cdots & \ddots & \cdots \\ \mathbf{A}^{N_c-1}\mathbf{B} & \mathbf{A}^{N_c-2}\mathbf{B} & \cdots & \mathbf{B} \\ \mathbf{A}^{N_c}\mathbf{B} & \mathbf{A}^{N_c-1}\mathbf{B} & \cdots & \mathbf{AB} \\ \vdots & \vdots & \ddots & \vdots \\ \mathbf{A}^{N_p-1}\mathbf{B} & \mathbf{A}^{N_p-2}\mathbf{B} & \cdots & \mathbf{A}^{N_p-N_c-1}\mathbf{B} \end{bmatrix}, \Phi = \begin{bmatrix} \mathbf{A} \\ \mathbf{A}^2 \\ \cdots \\ \mathbf{A}^{N_c} \\ \cdots \\ \mathbf{A}^{N_p} \end{bmatrix}$$

Solving the QP yields the optimal input sequence over the prediction horizon, as shown in Eq. (38). In implementation, only the first element is applied, and the optimization is repeated at the subsequent sampling instant, resulting in a receding-horizon strategy.

$$\mathbf{U}_k = [\tau(k), \tau(k+1), \cdots, \tau(k+N_c-1)]^T \tag{38}$$

4.2.5. Curvature compensation and heading saturation

On complex paths (e.g., trajectories with large curvature variations), relying solely on error feedback may lead to oscillations or tracking lag. Therefore, a curvature compensation term is introduced:

$$\kappa = \frac{d\psi_{path}}{ds} \tag{39}$$

where κ denotes the path curvature, ψ_{path} is the tangential heading angle of the reference path, a larger absolute value of κ indicates a sharper turn of the reference trajectory. The heading correction term is given by:

$$\Delta\psi = d\cdot\kappa \tag{40}$$

Combining these, the final desired heading is obtained as:

$$\psi_d = \psi_{path} - k_y e_y + \Delta\psi \tag{41}$$

In addition, to prevent excessively large control inputs from causing system instability, the heading is subjected to saturation:

$$\psi_d = \text{sat}(\psi_d, \psi_{max}) \tag{42}$$

where "sat(·)" denotes the saturation function.

This improved method can effectively suppress oscillations and enhance system stability and robustness under complex path conditions. With the above design, MPC is used only for heading dynamic optimization, while longitudinal control is handled by an independent module, thereby achieving effective control of computational complexity while ensuring control performance.

It should be noted that the proposed control signal is free of explicit singularities. The Frenet-frame error transformation is implemented through a rotation matrix, which is always nonsingular. The heading correction term is generated from the lateral error using a bounded and continuous nonlinear mapping, without division by the tracking error, relative distance, or velocity. The longitudinal speed coordination law is also based on direct error feedback and contains no singular terms. Moreover, the MPC-based heading controller is formulated as a constrained quadratic programming problem with input and input-increment constraints, and the final desired heading is saturated within a feasible range. Therefore, the designed control signal remains bounded and singularity-free in practical implementation.

4.2.6. Parameter selection and tuning methodology

The main controller parameters and their tuning basis are summarized in Table 1. The MPC horizons (N_p) and (N_c) are selected according to the sampling period, yaw-response characteristics, prediction accuracy, and real-time computational burden. The lateral-error gain (k_y) is used for heading-reference generation, while the longitudinal-error gain (λ) is adjusted for speed coordination and formation-spacing recovery. The input and input-increment constraints are determined based on actuator limitations, rate limits, and safe operating requirements of the physical USV platform.

Table 1
Controller parameter selection and tuning methodology.

Parameter	Value	Function	Selection/Tuning basis
T_s	0.1s	Sampling period	Determined according to sensor update rate, communication cycle, and real-time control implementation.
N_p	18	MPC prediction horizon	Sampling period, yaw-response time, prediction accuracy, and real-time computational burden.
N_c	3	MPC control horizon	Control update frequency, computational cost, and input smoothness.
λ	0.5	Longitudinal-error gain	Speed coordination.
k_y	3.9	Lateral-error gain	Heading-reference generation.
Input constraint	$\tau_u \in [0, 1500]$ $\tau_r \in [-3000, 3000]$	Actuator limitation	Determined from physical actuator capability.
Input-increment constraint	$\lvert\Delta\tau_u\rvert \le 150$ $\lvert\Delta\tau_r\rvert \le 300$	Input smoothness/ rate limit	Determined from actuator rate limit and safe operation requirements.

4.3. Summary

This section describes a decoupled formation control method based on Frenet-frame errors. Lateral and longitudinal errors are assigned to the heading and speed control channels, respectively, while MPC is applied only to the heading subsystem. In this way, the original coupled control problem is reduced to a lower-dimensional optimization problem. As a result, the computational burden is decreased, while the control performance remains acceptable, making the method suitable for real-time multi-USV applications.

5. Experimental validation

5.1. Experimental platform

To validate the proposed cooperative control strategy for multi-agent systems, a generic USV prototype experimental platform was developed. The platform is designed to meet the requirements of cooperative control experiments in nearshore and offshore environments, adopting a hierarchical architecture of a "shore-based command center–USV cluster" to support real-world validation of cooperative formation control algorithms.

In terms of communication and networking architecture, a mesh topology is employed to provide a robust wireless communication backbone with link redundancy and flexible routing among communication nodes. Each node is capable of transmitting real-time navigation data back to the shore-based command center for mission coordination and monitoring. To enhance communication reliability in complex marine environments, the platform integrates multiple communication links, including WiFi communication within a range of 100 m, a data radio with a coverage of up to 15 km, and a 4G communication module operating within public network coverage areas. This configuration establishes a hierarchical communication system that supports both line-of-sight and beyond-line-of-sight scenarios.

Regarding physical characteristics and maneuvering performance, the USV has a hull length of 5100 mm and a lightship weight of 290 kg, with a maximum speed of 6 knots. The endurance is 5 h at 6 knots and up to 25 h at 3 knots. The platform is suitable for sea states up to level 4. In terms of maneuverability, the minimum turning radius does not exceed 15 m, satisfying the requirements of formation reconfiguration and path-following experiments.

For navigation and attitude measurement performance, the system achieves a positioning accuracy better than 1 m. The heading accuracy of the attitude measurement unit is $\leq 0.06^\circ$ (RMS), while the roll and pitch accuracies are $\leq 0.02^\circ$ (RMS), providing high-precision state feedback for the MPC control algorithm.

The main parameters and performance specifications of the USV experimental platform are summarized in Table 2.

5.2. Field experiment setup

In this study, three USVs were deployed for field validation experiments. The sea trials were conducted in the coastal waters near Weihai City, Shandong Province, China, specifically in the vicinity of the Yuanyao Wharf Experimental Site. The experimental area is bounded by the following geographic coordinates:(37.5485131°N, 122.0898015°E), (37.5466083°N, 122.0882137°E), (37.5417274°N, 122.1020607°E), and(37.5481761°N, 122.1062481°E).

The sea trials consisted of two main components:

Data acquisition for model identification, aimed at obtaining hydrodynamic and motion data for system parameter estimation; Formation and cooperative control experiments, conducted to validate the proposed cluster control strategy under real marine conditions.

Both experimental campaigns were carried out in nearshore waters with an average depth of approximately 8 m. During the test period, the sea state was approximately level 2–3, corresponding to mild wave disturbances and moderate wind conditions. These environmental conditions introduced realistic external disturbances, thereby providing a practical testbed for evaluating system robustness and control performance.

5.3. System identification results

To obtain high-fidelity hydrodynamic parameters for the USV dynamic model, real sea-trial data were collected for system identification. The onboard integrated navigation system provides accurate attitude and position measurements, while the internal logging data additionally record the thrust and yaw moment commands issued by the main control system (see Figs. 5–7).

As illustrated in Fig. 8, control commands generated at the ground control station are sent to the onboard antenna unit through a wireless data link. The communication module within the antenna unit converts network data into serial signals and forwards them to the main control board. Based on the received commands, the main controller computes the required thrust and yaw moment and sends them to the motor driver board. The driver board applies a thrust allocation matrix to transform the commanded forces and moments into PWM duty cycles, thereby actuating the propulsion motors.

During operation, the motion states of the USVs are obtained from the onboard navigation system and sent in real time to the sensor board. The data are then collected and stored by the main controller for later processing.

Table 2
USV parameter table.

Name	Parameters
Dimensions	5100 mm
Weight(in air)	290 kg
Navigation time	5 h@6knots,25 h@3knots
Max.Speed	6knots
Localization Accuracy	≤1 m
Turning radius	≤15 m
Operating sea conditions	≤level 4
Network Topology	Mesh Networking
Attitude sensor performance	Heading accuracy: ≤0.06° (RMS) Roll and pitch angle accuracy: ≤0.02° (RMS)
Communication	WiFi:100 m; Digital transmission station:15 km; 4G:the maritime coverage region of the base station;

With this communication setup, straight-line constant-speed tests and turning maneuvers were carried out separately for each USV. After preprocessing the data, the least-squares method was used for parameter estimation. The model parameters were determined by minimizing the root mean square error (RMSE) between the measured and predicted states. The identified dynamic models for the surge and yaw motions of the three USVs are given as follows:

$$\begin{cases} 246.13\dot{u} + 829.62u - 22.78u|u| - 31.68 = \tau_u \\ 9.17\dot{r} + 70.49r + 1.29r|r| - 26.49 = \tau_r \\ 106.58\dot{u} + 471.45u + 134.96u|u| + 192.81 = \tau_u \\ 8.01\dot{r} + 59.07r + 2.05r|r| - 2.73 = \tau_r \\ 78.27\dot{u} + 529.53u + 44.93u|u| + = \tau_u \\ 9.99\dot{r} + 41.27r + 5.83r|r| + 26.57 = \tau_r \end{cases} \tag{43}$$

The above formulation yields model parameters identified from extensive experimental datasets by minimizing the root mean square error (RMSE) between the model output and measurements. Specifically, the measured motion signals are substituted into the left-hand side of Eq. (9) to compute the estimated forces and moments, which are then compared with the actual thrust and yaw moment obtained from experiments.

As illustrated in Figs. 9–11, the identified model outputs exhibit strong agreement with the measured thrust and yaw moment, indicating that the proposed identification procedure achieves high modeling accuracy.

To further verify the reliability of the identified parameters and the excitation richness of the experimental data, additional validation tests were conducted using sinusoidal excitation inputs. Specifically, sinusoidal thrust inputs were applied to the surge subsystem, while sinusoidal yaw-moment inputs were applied to the yaw subsystem. The measured input signals were then substituted into the identified surge and yaw dynamic models to obtain the model-predicted surge velocity and yaw rate, which were compared with the corresponding measured responses. As shown in Figs. 12 and 13, the predicted responses exhibit good agreement with the measured responses under sinusoidal excitation conditions. This indicates that the identified parameters can effectively characterize the nominal surge and yaw dynamics of the practical USV platform and that the collected experimental data provide sufficient excitation richness for the control-oriented identification task.

5.4. Monte Carlo robustness evaluation

To further evaluate the robustness of the proposed Frenet-frame-based MPC formation control framework, Monte Carlo simulations were conducted and compared with a sliding mode control method. The simulation scenario was set as a triangular formation tracking task. For each control method, 100 independent trials were performed under mild, medium, and severe uncertainty levels, corresponding to random perturbation ranges of (±10%), (±30%), and (±50%) in the model parameters, respectively. Meanwhile, measurement noise, sensor quantization/dead-zone effects, actuator saturation, and input rate limits were kept consistent across all simulation groups to evaluate the robustness of the controllers under practical non-ideal conditions.

In the Monte Carlo simulations, the model parameters of the three USVs were randomly perturbed, noise was added to the position and heading measurements, and sensor quantization and dead-zone effects were considered. The thrust and yaw moment were constrained within their feasible operating ranges, and input-increment constraints were imposed to avoid abrupt changes in the control inputs. Fig. 14 presents the distribution of the 2D RMSE under different uncertainty levels. These results provide a more comprehensive evaluation of the robustness of the proposed method in terms of parameter perturbations, measurement noise, actuator constraints, and sensor non-idealities, and provide simulation support for the subsequent real-sea experimental validation (see Fig. 15).

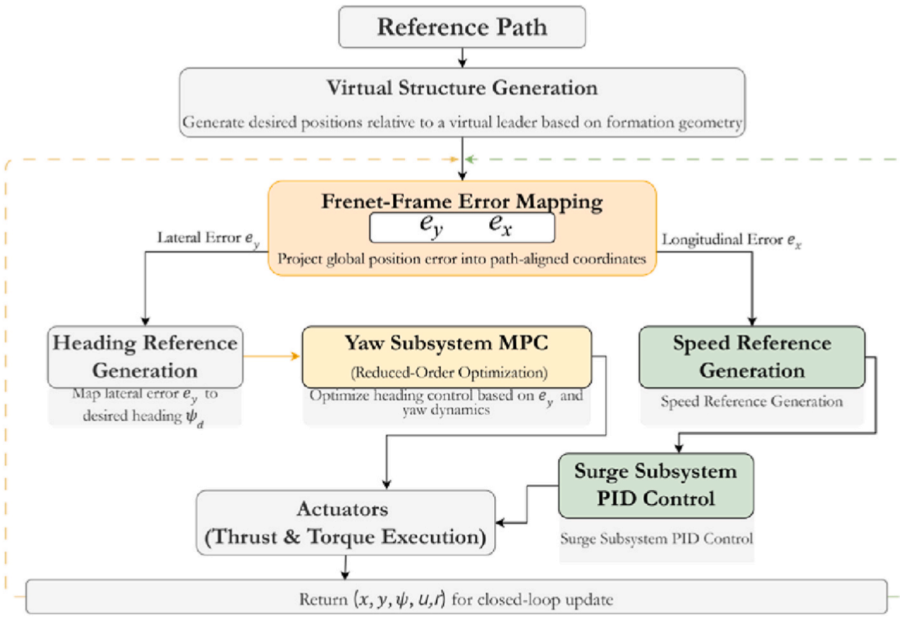

Fig. 5. Formation control framework for Multi-USVs.

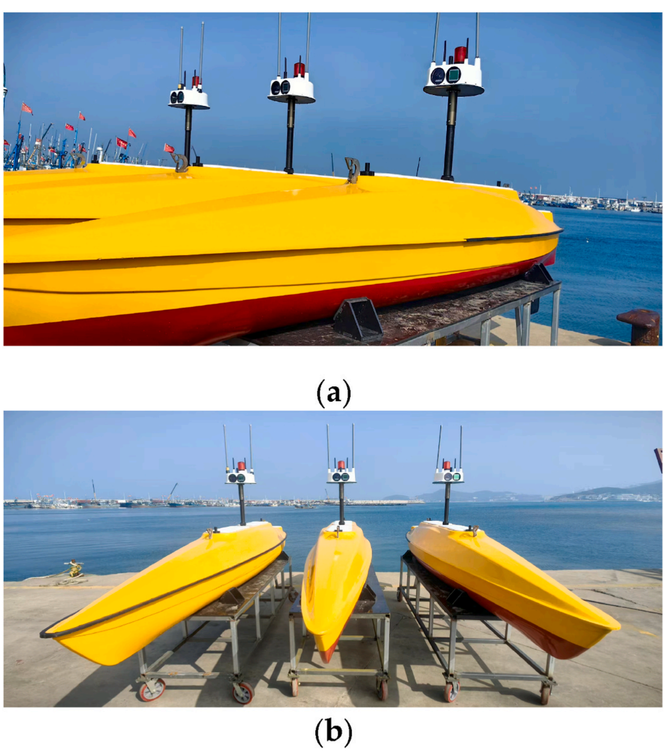

Fig. 6. The USV prototype.

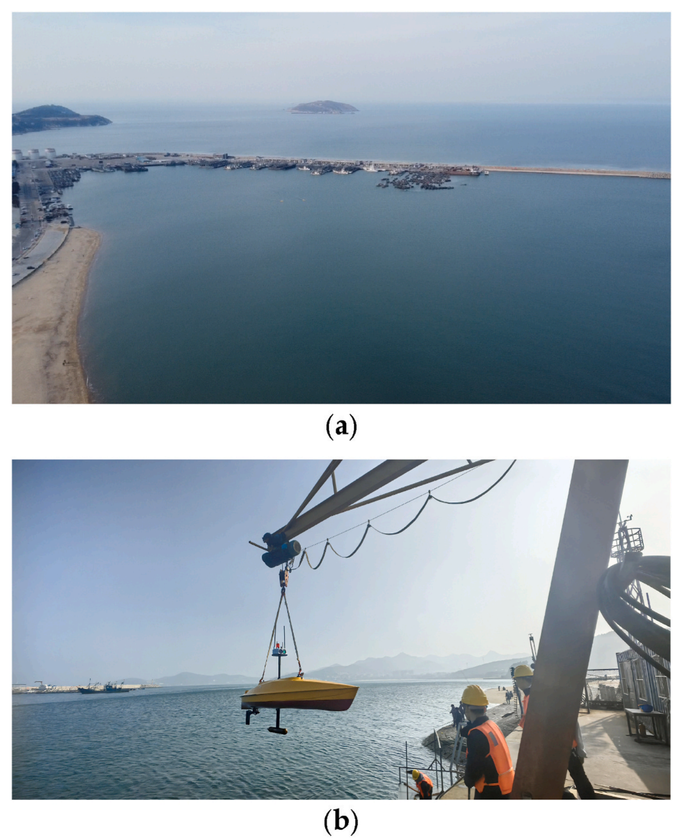

Fig. 7. Experimental setup.

5.5. Formation control experiments

Multi-USV sea trials were conducted to evaluate the Frenet-frame-based decoupled formation control method under real marine conditions. Two formation types were tested: line formation and triangular formation. In both, the USVs followed a figure-eight trajectory, keeping even spacing along the path's tangential direction and a fixed longitudinal separation.

A simulated single-USV propeller-failure scenario was also tested. In this test, the propeller of one USV was intentionally stopped during the mission to simulate the loss of propulsion capability. The objective was to examine whether the remaining USVs could continue the path-following task after one vehicle became unable to follow the commanded trajectory.

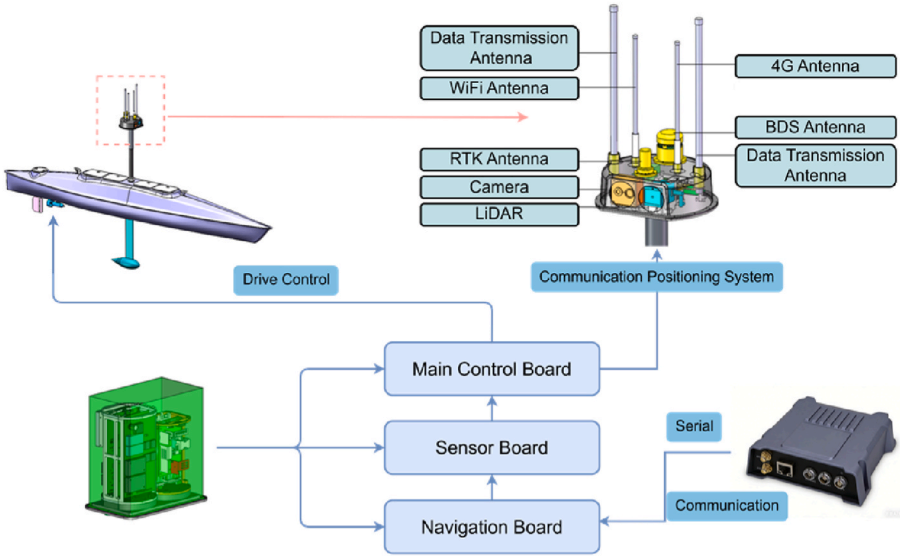

Fig. 8. Data acquisition process during system identification.

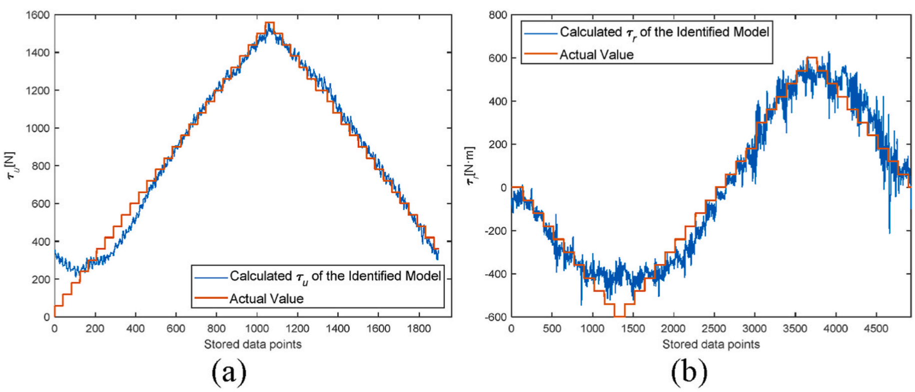

Fig. 9. Identification results versus ground truth for USV1: (a) Thrust; (b) Torque.

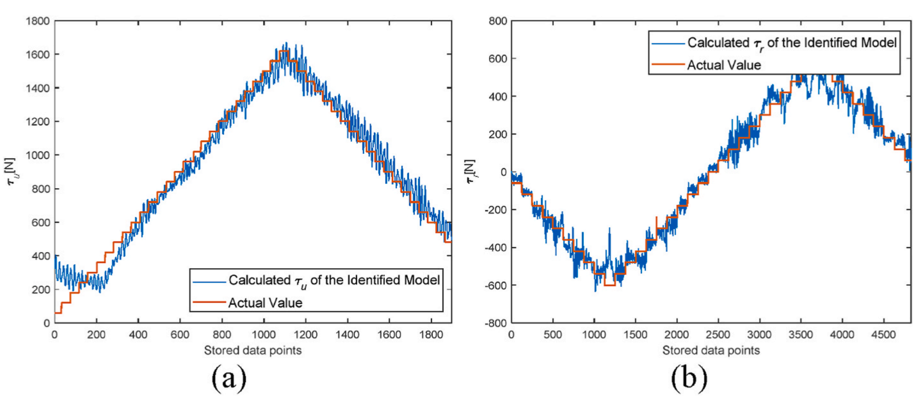

Fig. 10. Identification results versus ground truth for USV2: (a) Thrust; (b) Torque.

5.5.1. Reference trajectory design and formation configuration based on virtual structure

The reference path is defined as a figure-eight trajectory, as expressed in the equation. The trajectory parameter is set to (a = 150), resulting in a lateral range of ([−150 m, 150 m]) and a longitudinal range of ([−53 m, 53 m]), which effectively characterizes path-following problems under continuously varying curvature conditions.

$$\begin{cases} x = a \times \cos(t)/(1 + \sin(t) \times \sin(t)) \\ y = a \times \sin(t) \times \cos(t)/(1 + \sin(t) \times \sin(t)) \end{cases} \tag{44}$$

where x and y denote the coordinates of the reference trajectory in the Earth-fixed frame, a is the trajectory scale parameter, and λ is the path parameter. In this study, a is set to 150, resulting in a lateral range of approximately [-150 m, 150 m] and a longitudinal range of

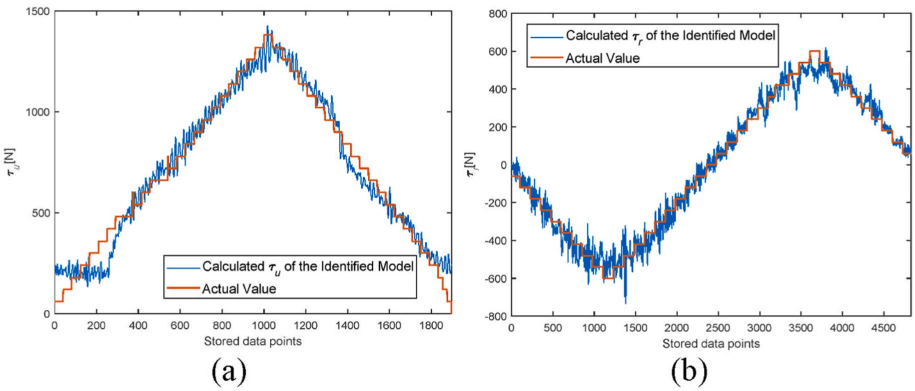

Fig. 11. Identification results versus ground truth for USV3: (a) Thrust; (b) Torque.

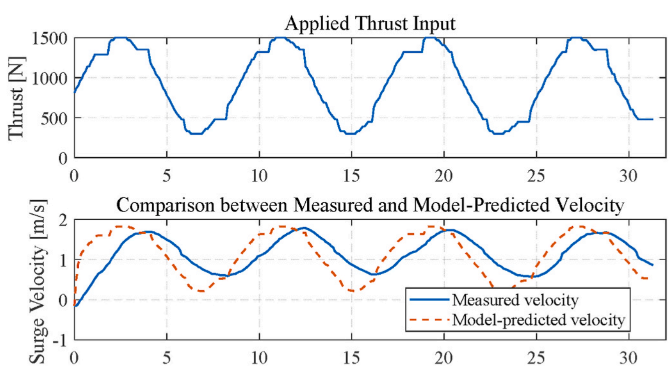

Fig. 12. Surge-model response under sinusoidal thrust excitation.

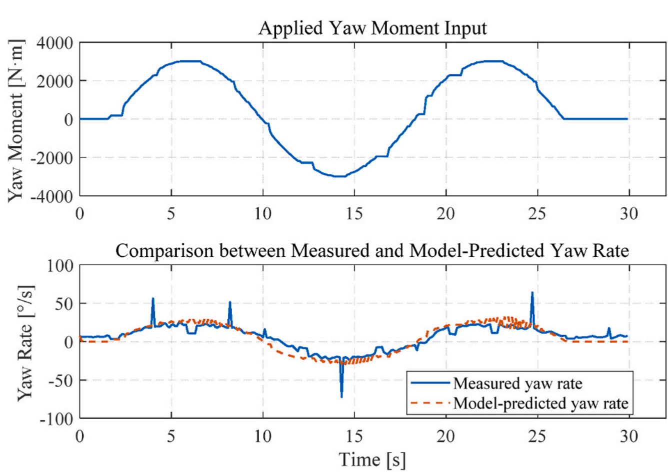

Fig. 13. Yaw-model response under sinusoidal yaw-moment excitation.

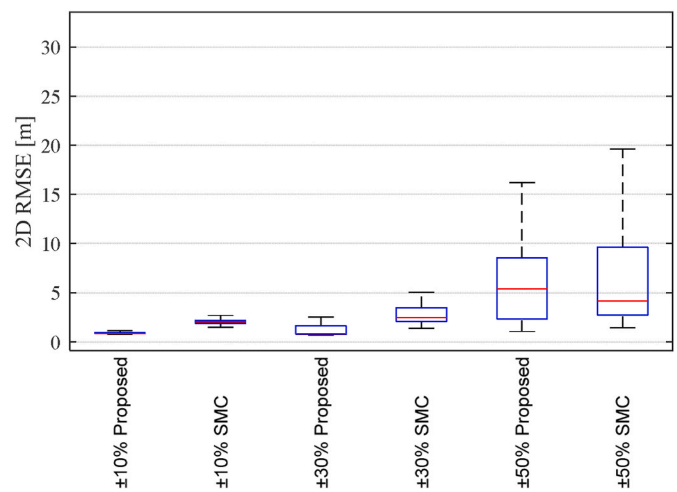

Fig. 14. Monte Carlo 2D RMSE under different uncertainty levels.

Fig. 15. Real-life photo of the line-formation figure-8 path-following test.

approximately [-53 m, 53 m].

Within the virtual structure framework, the middle USV is designated as the leader, with its position denoted as $\mathbf{p}_1$, and it moves along the aforementioned figure-eight trajectory. The desired positions of the follower USVs are constructed based on the tangential and normal directions of the reference path. The expressions for the line formation and triangular formation are given in Eqs. (43) and (44), respectively. Here, d denotes the formation scale parameter, which is set to ($d = 15$).

$$\mathbf{p}_2 = \mathbf{p}_1 + d{\cdot}\mathbf{n}, \mathbf{p}_3 = \mathbf{p}_1 - d\,{\cdot}\mathbf{n} \tag{45}$$

$$\mathbf{p}_2' = \mathbf{p}_1 - \frac{1}{2}d{\cdot}\mathbf{t} + \frac{\sqrt{3}}{2}d{\cdot}\mathbf{n}, \mathbf{p}_3' = \mathbf{p}_1 - \frac{1}{2}d{\cdot}\,\mathbf{t} - \frac{\sqrt{3}}{2}d{\cdot}\,\mathbf{n} \tag{46}$$

This method embeds the formation structure into the geometric properties of the path, enabling real-time adaptive adjustment of the formation with respect to the path direction. Compared with fixed formation strategies, it exhibits stronger path adaptability and improved motion consistency.

5.5.2. *Line-formation figure-eight path-following experiment*

As shown in Fig. 16, a real-world snapshot of the line-formation figure-eight path-following experiment is presented. In this experiment, three USVs form a line formation, distributed along the tangential direction of the reference path while maintaining a fixed longitudinal spacing during motion. Fig. 18 illustrates the formation trajectories, Fig. 19 presents zoomed-in views of the start and end regions along with

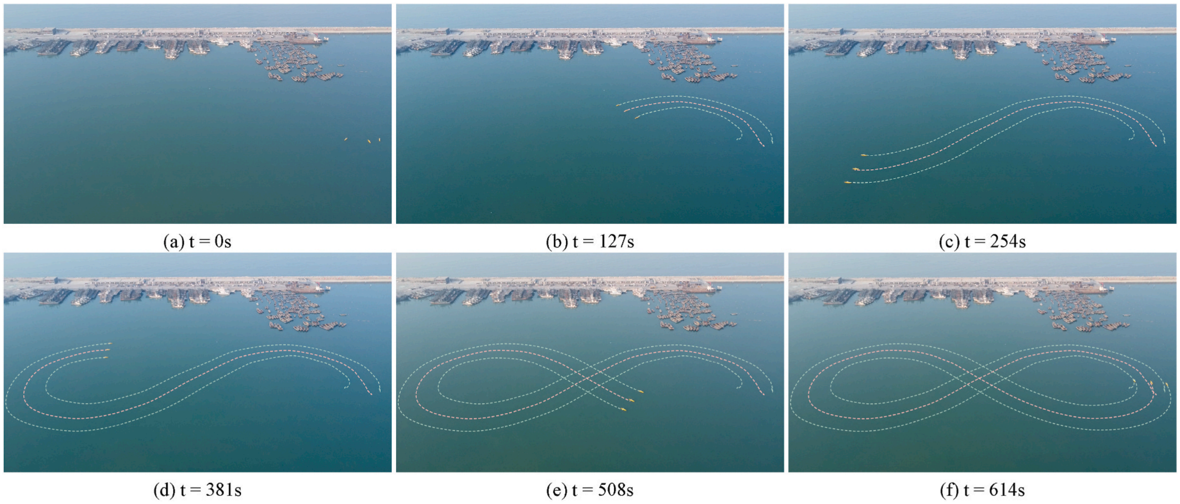

Fig. 16. Time-sequence snapshots of the three-USV formation during the "8"-shaped path-following experiment with a line formation.

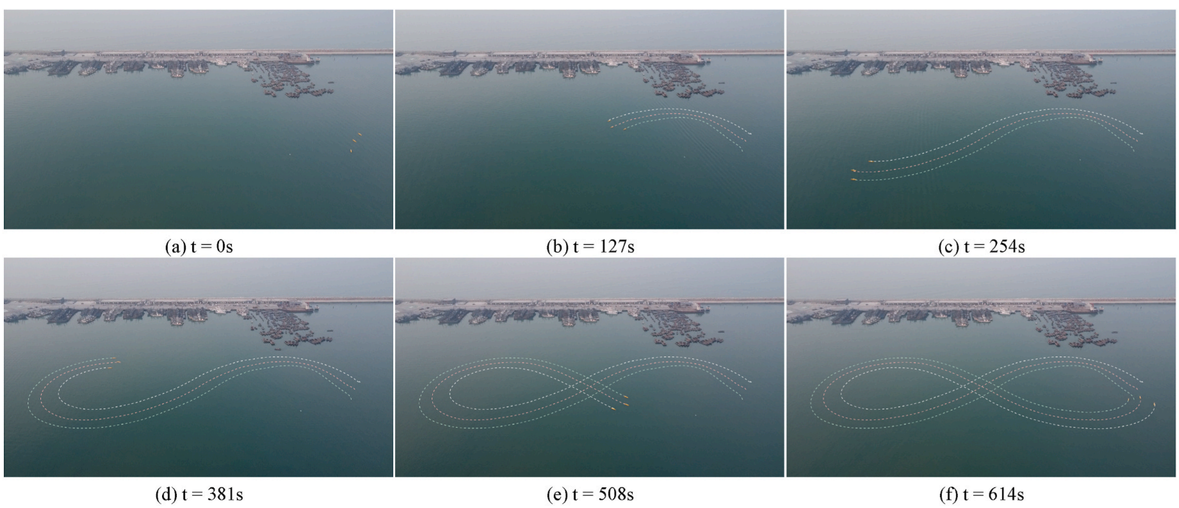

Fig. 17. Time-sequence snapshots of the three-USV formation during the "8"-shaped path-following experiment with a triangular formation.

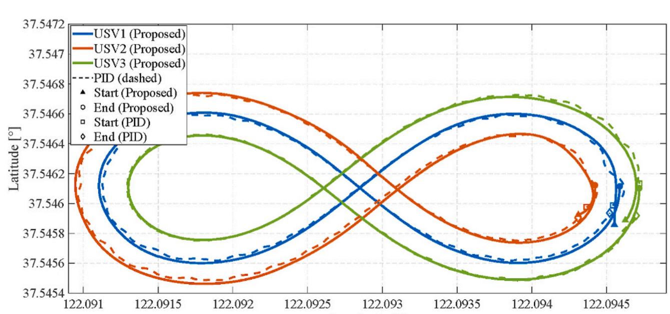

Fig. 18. Trajectories of the USV line formation.

inter-vehicle distance variations, and Fig. 21 shows the heading angles of the three USVs (see Fig. 20) (see Figs. 17 and 20).

During the experiment, the position and attitude of each USV are obtained from a GPS/INS integrated navigation system and transmitted to the shore-based control station via a 4G link at 10 Hz. Based on the Frenet frame, the tracking error is decoupled into lateral error e_y and longitudinal error e_x. The lateral error is used to generate the heading reference and is regulated by MPC, while the longitudinal error is controlled by a PID controller to maintain the desired formation spacing. Under this framework, each USV operates independently based on its own error without requiring communication topology or neighbor information exchange.

Fig. 18 shows that the method enables stable tracking of the figure-eight trajectory, with all three USVs maintaining good formation consistency throughout the experiment.

Smooth trajectory transitions and stable performance are observed even in regions with large curvature variations. In contrast, the PID method exhibits more noticeable trajectory deviations in local regions (Fig. 18).

Table 3 lists the statistical outcomes for inter-vehicle distances. The proposed method keeps the desired spacing well, with average distances close to the set values. It also beats the PID method in terms of RMSE and maximum deviation, showing better formation-keeping ability under complex paths. Table 4 gives a summary of the path-tracking errors. The proposed method performs better in lateral error, which confirms the value of using MPC for heading control. Meanwhile, the longitudinal error remains comparable between the two methods, since both rely on PID for that part. Thanks to the decoupled control design, the overall tracking consistency is improved with the proposed method.

It should be noted that the USVs did not start from ideal initial states in this experiment. As shown in the zoomed-in start region in Fig. 19 and

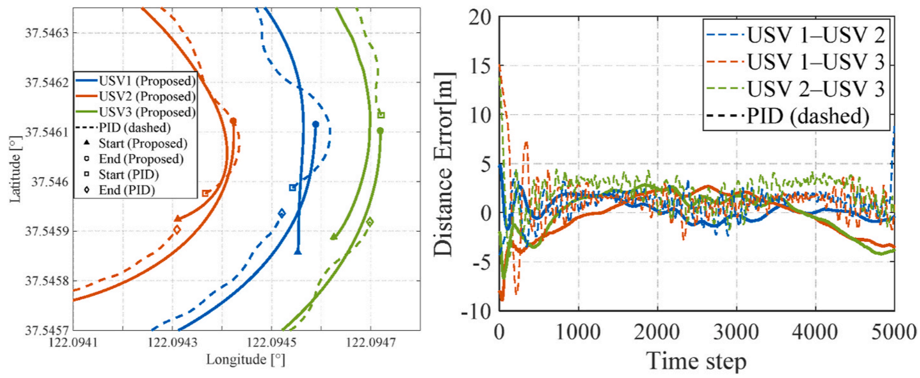

Fig. 19. Zoomed-in Views of Its Start and End Regions and Inter-vehicle distances among the three USVs.

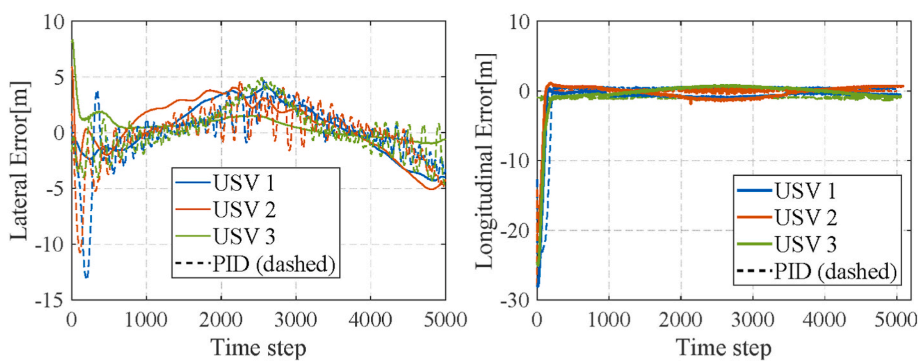

Fig. 20. USV lateral and longitudinal error graph.

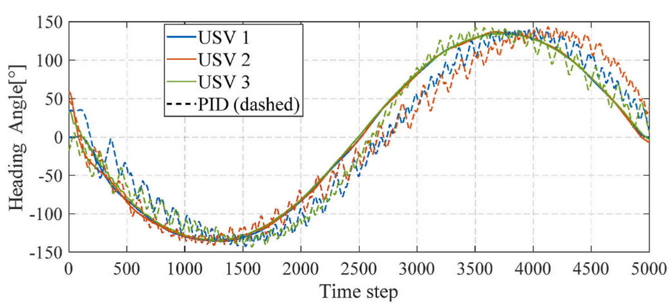

Fig. 21. Heading angles of the three USVs.

Table 3
Inter-vehicle distance statistics of the USV formation.

Method	Pair	Mean Distance (m)	RMSE (m)	Max Deviation (m)
Proposed	USV1-USV2	**15.2770**	**1.0768**	**19.8087**
Proposed	USV1-USV3	**14.7160**	**2.2590**	**17.6805**
Proposed	USV2-USV3	**30.0203**	**2.1907**	**32.8456**
PID	USV1-USV2	15.9804	1.7024	23.8398
PID	USV1-USV3	16.1762	2.6629	30.1118
PID	USV2-USV3	32.1884	2.8191	43.7558

the heading-angle responses in Fig. 21, the three USVs had noticeable initial position/formation deviations and relatively large initial heading errors. Nevertheless, the proposed controller successfully regulated the USVs toward the desired figure-eight trajectory and maintained stable formation distances, demonstrating its effectiveness under large initial conditions.

Table 4
Path-following error statistics of the USV formation.

Method	Lateral RMSE (m)	Longitudinal RMSE (m)
Proposed	**2.0760**	**2.6842**
PID	2.4074	2.7504

5.5.3. Triangular-formation figure-eight path-following experiment

To further verify the adaptability of the proposed Frenet-frame MPC formation control framework to different formation configurations, a triangular-formation figure-eight path-following sea trial was conducted, with the conventional sliding mode control (SMC) method used for comparison. In the experiment, the desired position of each USV was updated in real time according to the tangential and normal directions of the figure-eight reference path, allowing the formation configuration to adapt to the path direction. This design is consistent with the Frenet-frame error modeling method, in which the global position error is decomposed into longitudinal and lateral errors, which are used for speed coordination and heading regulation, respectively.

Figs. 22 and 23 show the overall trajectories of the triangular-formation figure-eight path-following experiment and the zoomed-in views of the start and end regions, respectively. The results indicate that all three USVs were able to follow their respective desired trajectories and maintain a stable triangular formation during the continuously varying curvature segments. Compared with the conventional SMC method, the trajectories obtained by the proposed method are smoother and closer to the desired trajectories. In particular, better spatial consistency is observed during the initial formation establishment stage and the terminal convergence stage.

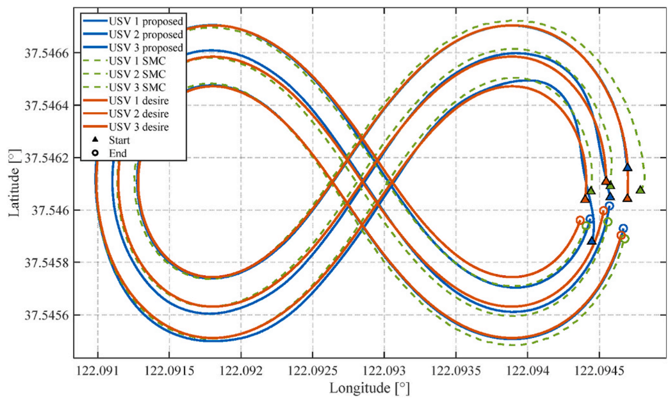

Fig. 22. Trajectories of the USV triangular formation.

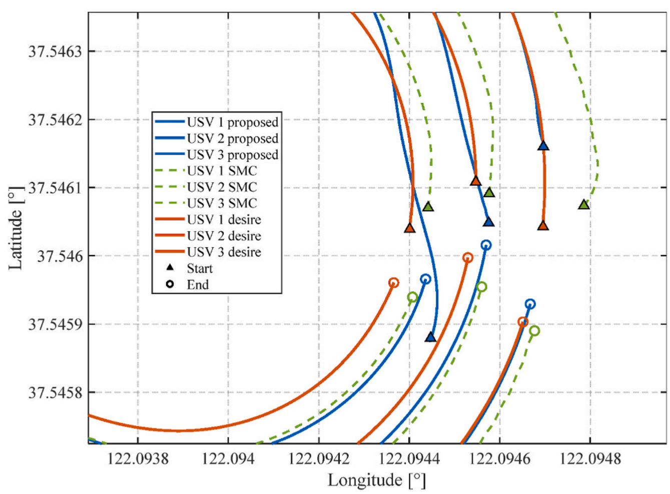

Fig. 23. Zoomed-in views of its start and end regions.

Table 5 presents the RMSE comparison of formation errors over different evaluation intervals. Since the three USVs had initial heading and formation-position deviations at the beginning of the sea trial, the full-period error includes the transient effect caused by formation establishment. Over the full period, the 2D RMSE of the proposed method is 2.5715 m, which is lower than that of the SMC method, 2.8778 m, indicating better overall formation-keeping performance. After removing the initial transient stage, the longitudinal RMSE, lateral RMSE, and 2D RMSE of the proposed method are 0.4404 m, 1.5466 m, and 1.6493 m, respectively, all of which are smaller than those of the SMC method, namely 0.8405 m, 2.3273 m, and 2.4967 m. This demonstrates that the proposed method achieves higher formation-keeping accuracy during the stable formation stage. The longitudinal and lateral error responses shown in Fig. 24 further support this conclusion.

Fig. 25 and Table 6 present the heading-angle responses of the three USVs and the heading smoothness metrics, respectively. The Diff_RMS, Total_Var, and Osc_RMS of the proposed method are 0.1752, 557.6, and 0.3246, respectively, all of which are lower than those of the SMC method, namely 0.2938, 1025.1, and 1.0354. These results indicate that the proposed method can effectively reduce heading variation and high-frequency oscillations, thereby achieving smoother heading responses. This advantage mainly benefits from the predictive optimization mechanism of MPC and the input-increment constraints, which suppress abrupt control changes and reduce the chattering commonly observed in conventional sliding mode control.

Table 5
RMSE comparison of formation errors over different evaluation intervals.

Evaluation interval	Method	Long_RMSE [m]	Lateral_RMSE [m]	2D_RMSE [m]
After initial transient	Proposed	**0.4404**	**1.5466**	**1.6493**
After initial transient	SMC	0.8405	2.3273	2.4967
Full period	Proposed	1.9505	**1.5826**	**2.5715**
Full period	SMC	**1.0979**	2.6531	2.8778

In summary, the triangular-formation figure-eight path-following sea trial verifies the adaptability and engineering feasibility of the proposed Frenet-frame MPC formation control framework under a complex formation configuration. The experimental results demonstrate that the proposed method can achieve stable trajectory tracking, improved formation-keeping accuracy, and smooth heading regulation on a complex figure-eight path, indicating good formation-configuration generalization capability and practical application potential.

5.5.4. *Single-USV propeller-failure scenario and mission-continuation test*

To assess robustness and fault tolerance under complex real-world conditions, formation navigation experiments were performed under various fault scenarios, including single-USV failures and formation reconfiguration.

The experimental results are shown in Figs. 26 and 27. When any individual USV fails, the remaining vehicles are able to continue the path-following task without requiring global communication reconfiguration (Fig. 26). In the case of leader failure, the system can perform role reassignment, where another USV takes over the leading role and maintains formation operation (Fig. 27(a)). In addition, the formation can be dynamically reconfigured during navigation, achieving a smooth transition from triangular to line formation without introducing noticeable trajectory oscillations or instability (Fig. 27(b)).

These results indicate that the proposed Frenet-frame-based decoupled control method not only achieves satisfactory path-following and formation-keeping performance, but also maintains stable operation under individual failures and structural changes, indicating strong robustness and practical applicability.

5.6. *Discussion*

Based on the sea-trial results, the advantages and limitations of the proposed Frenet-frame-based MPC formation control framework are discussed.

The main advantage of the proposed method lies in its decoupled control structure. By introducing the Frenet frame, the global formation tracking error is decomposed into lateral and longitudinal components, which improves the geometric clarity of the error representation and reduces the coupling between heading regulation and speed coordination. Moreover, MPC is applied only to the heading subsystem rather than to the full multi-USV formation model. This reduced-order design decreases the dimension of the online optimization problem and lowers the computational burden while retaining the prediction and constraint-handling capabilities of MPC. In addition, the shore-based centralized control-decision structure avoids strong dependence on explicit inter-USV control topology and facilitates real-sea experimental deployment.

The proposed method also has some limitations. The Frenet-frame error calculation depends on the accuracy of position and heading measurements, and the control-oriented reduced-order prediction model simplifies some high-order hydrodynamic coupling terms. This simplification is mainly adopted to meet the real-time computational requirements of multi-USV formation control. To verify the reliability of the simplified model, additional excitation tests were conducted, and the model-predicted surge velocity and yaw-rate responses were compared with the measured responses. The results indicate that the reduced-order model can capture the main surge and yaw dynamics of the USV platform and satisfy the requirements of controller design and sea-trial validation in this study.

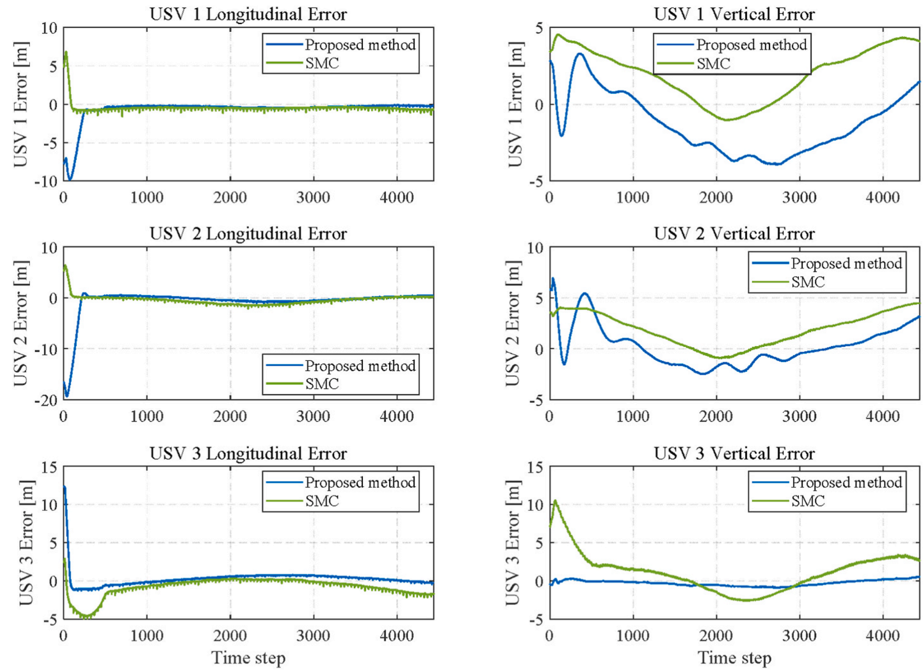

Fig. 24. USV lateral and longitudinal error graph.

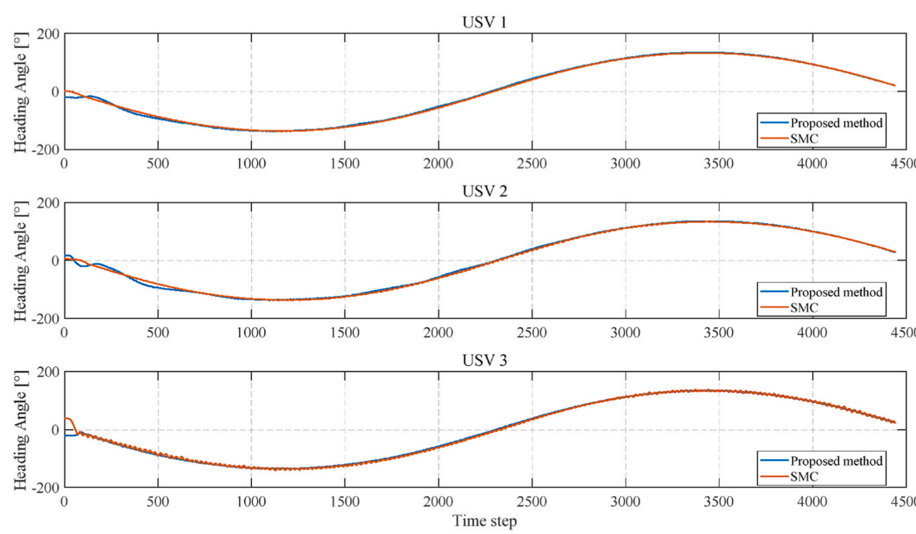

Fig. 25. Heading angles of the three USVs.

Table 6
Comparison of heading oscillation metrics between the proposed method and conventional SMC.

Method	Diff_RMS	Total_Var	Osc_RMS
Proposed	**0.1752**	**557.6**	**0.3246**
SMC	0.2938	1025.1	1.0354

Overall, the proposed framework achieves a balance among geometric error interpretability, computational efficiency, constraint handling, and engineering applicability. Further validation under harsher sea conditions and more aggressive maneuvers will be considered in future work.

6. Conclusions

This paper proposed a Frenet-frame-based formation control method for multiple underactuated USVs under complex path-following conditions. By introducing Frenet error decomposition and a hierarchical control structure, the coupled formation tracking problem was simplified into coordinated heading and speed control, reducing the complexity of controller design and online optimization.

Real-sea experiments on a figure-eight trajectory verified that the proposed method can achieve accurate trajectory tracking and stable formation keeping under continuously varying curvature. The fault scenario further demonstrated its practical robustness and adaptability in multi-USV cooperative missions.

Overall, the proposed method offers a concise and feasible solution for engineering applications of USV formation control in real marine environments.

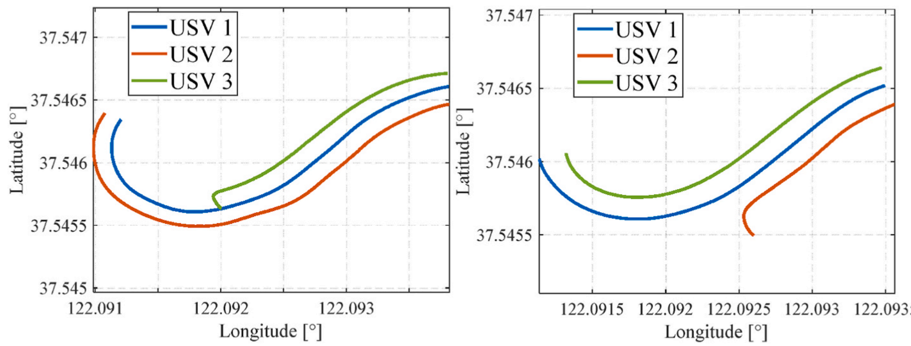

Fig. 26. Fault-tolerant navigation under single-USV failures: (a) USV3 failure, where USV1 and USV2 continue the mission; (b) USV2 failure, where USV1 and USV3 continue the mission.

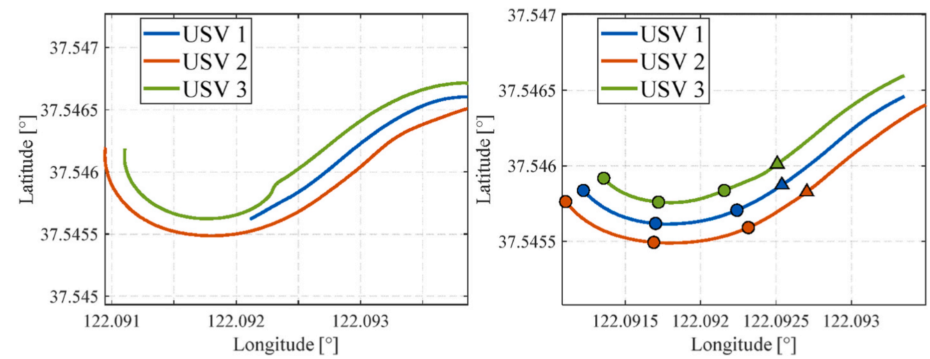

Fig. 27. Fault recovery and formation reconfiguration: (a) leader replacement after USV1 failure, where USV3 takes over the leading role; (b) formation transition from triangular formation to line formation during navigation.

CRediT authorship contribution statement

Shunli Wang: Conceptualization, Formal analysis, Investigation, Methodology, Resources, Software, Validation, Writing – original draft, Writing – review & editing. **Xiufen Ye:** Data curation, Funding acquisition, Project administration, Visualization. **Shuxiang Guo:** Conceptualization, Methodology, Resources, Visualization. **Chunying Li:** Data curation, Project administration. **Ronghao Zhang:** Formal analysis, Methodology, Visualization, Writing – original draft. **Xihuan Hou:** Investigation, Supervision, Writing – original draft.

Declaration of competing interest

The authors declare that they have no known competing financial interests or personal relationships that could have appeared to influence the work reported in this paper.

Acknowledgment

This research was supported by the Guangdong Basic and Applied Basic Research Foundation General Program under Grant 2025A1515011007, Guangdong, China, in part by the Shenzhen Science and Technology Program under Grant RCBS20231211090725048, in part by the High level of special funds from Southern University of Science and Technology under Grant G03034K003, Shenzhen, China.

Appendix A. Supplementary data

Supplementary data to this article can be found online at https://doi.org/10.1016/j.oceaneng.2026.127083.

References

Chang, W.-J., Lin, Y.-H., Lee, Y.-C., Ku, C.-C., 2024. Investigating formation and containment problem for nonlinear multiagent systems by interval Type-2 fuzzy sliding mode tracking approach. IEEE Trans. Fuzzy Syst. 32, 4163–4177. https://doi.org/10.1109/TFUZZ.2024.3387045.

Chang, Z., Zong, G., Wang, W., Yue, M., Zhao, X., 2025. Formation control and obstacle avoidance design for networked USV swarm with exogenous disturbance under intermittent communication. IEEE Trans. Network Sci. Eng. 12, 3234–3243. https://doi.org/10.1109/TNSE.2025.3558548.

Dong, Z., Liu, W., Ding, Y., Lu, S., Hu, Z., Liu, Y., 2025. Time-varying formation trajectory tracking scheme for underactuated USVs based on adaptive sliding mode control with improved guidance strategy. Ocean Eng. 331, 121340. https://doi.org/10.1016/j.oceaneng.2025.121340.

Fan, Y., Huang, H., Tan, Y., 2019. Robust adaptive path following control of an unmanned surface vessel subject to input saturation and uncertainties. Appl. Sci. 9, 1815. https://doi.org/10.3390/app9091815.

Han, X., Zhang, X., 2022. Tracking control of ship at sea based on MPC with virtual ship bunch under Frenet frame. Ocean Eng. 247, 110737. https://doi.org/10.1016/j.oceaneng.2022.110737.

Huang, J., Zhang, Y., Yang, X., Luo, Z., 2020. Transfer function model identification based on improved least square method. In: 2020 Chinese Automation Congress (CAC), pp. 487–491. https://doi.org/10.1109/CAC51589.2020.9327337.

Hung, N., Rego, F., Quintas, J., Cruz, J., Jacinto, M., Souto, D., Potes, A., Sebastiao, L., Pascoal, A., 2023. A review of path following control strategies for autonomous robotic vehicles: theory, simulations, and experiments. J. Field Robot. 40, 747–779. https://doi.org/10.1002/rob.22142.

Källström, C.G., 1996. Guidance and control of ocean vehicles: by Thor I. Fossen. Automatica 32, 1235. https://doi.org/10.1016/0005-1098(96)82331-4. Wiley, Chichester (1996). ISBN 0-471-94113-1.

Li, W., Zhang, J., Wang, F., Zhou, H., 2023. Model predictive control based on state space and risk augmentation for unmanned surface vessel trajectory tracking. J. Mar. Sci. Eng. 11, 2283. https://doi.org/10.3390/jmse11122283.

Liao, Y., Zhang, M., Wan, L., 2015. Serret-Frenet frame based on path following control for underactuated unmanned surface vehicles with dynamic uncertainties. J. Cent. South Univ. 22, 214–223. https://doi.org/10.1007/s11771-015-2512-z.

Lin, Y.-H., Chang, W.-J., Lee, Y.-C., Aslam, M., Ku, C.-C., 2025. Computational design of interval Type-2 fuzzy control for formation and containment of multi-agent systems with collision avoidance capability. https://doi.org/10.32604/cmes.2025.067464.

Liu, C., Hu, Q., Wang, X., 2021. Distributed guidance-based formation control of marine vehicles under switching topology. Appl. Ocean Res. 106, 102465. https://doi.org/10.1016/j.apor.2020.102465.

Liu, T., Zaopeng, D., Du, H., Song, L., Mao, Y., 2017. Path following control of the underactuated USV based on the improved line-of-sight guidance algorithm. Pol. Marit. Res. 24. https://doi.org/10.1515/pomr-2017-0001.

Liu, Y., Xu, X., Li, G., Lu, L., Gu, Y., Xiao, Y., Sun, W., 2025. Cooperative patrol control of multiple unmanned surface vehicles for global coverage. J. Mar. Sci. Eng. 13, 584. https://doi.org/10.3390/jmse13030584.

Naderolasli, A., 2026a. Fixed-time constrained platoon formation control of autonomous surface vessels with limited field-of-view sensors and saturated actuators. Ocean Eng. 348, 123996. https://doi.org/10.1016/j.oceaneng.2025.123996.

Naderolasli, A., 2026b. Adaptive finite-time fractional-order sliding-mode control of a state-constraint inverted pendulum cart system with limited sensing range. J. Vib. Control. https://doi.org/10.1177/10775463261417386, 10775463261417386.

Naderolasli, A., 2026c. Constrained adaptive fractional-order sliding-mode controller for stabilizing the two-degree-of-freedom gimbal system with limited field-of-view sensors: theoretical and experimental discussion. J. Field Robot. n/a. https://doi.org/10.1002/rob.70204.

Rui, G., Yanqing, J., Hang, L., Jingxuan, G., Yiyang, Z., Jialin, W., Yixian, Z., Teng, M., Yueming, L., Jian, C., Ye, L., 2026. Formation control for multi-autonomous underwater vehicles in cooperative underwater topography detection: methods and validation. J. Field Robot. 43, 779–795. https://doi.org/10.1002/rob.70061.

Shi, J., Ye, M., 2024. Distributed optimal formation control for unmanned surface vessels by a regularized game-based approach. IEEE/CAA J. Autom. Sin. 11, 276–278. https://doi.org/10.1109/JAS.2023.123930.

Song, X., Wu, C., Lam, H.-K., Wang, X., Song, S., 2025. Adaptive fuzzy predefined-time cooperative formation control for multiple USVs with universal global performance constraints. IEEE Trans. Intell. Transport. Syst. 26, 10725–10735. https://doi.org/10.1109/TITS.2025.3547955.

Su, Y., Yu, R., Ye, P., Li, T., 2025. Singularity-free fixed-time cooperative tracking control of unmanned surface vehicles with model uncertainties. J. Mar. Sci. Eng. 13, 1791. https://doi.org/10.3390/jmse13091791.

Sun, Z., Zhang, L., Huang, B., Zhu, C., 2026. Local node-driven distributed formation control for USVs: an LMPC-based safety-enhanced mechanism. IEEE Internet Things J. 1–1. https://doi.org/10.1109/JIOT.2026.3680274.

Suo, Y., Zhu, K., Wang, W., Yang, S., Cui, L., 2026. A novel action-aware multi-agent soft actor–critic algorithm for tight formation control in USV swarm. J. Mar. Sci. Eng. 14, 450. https://doi.org/10.3390/jmse14050450.

Wang, C., Wang, Y., Han, Q.-L., Wu, Y., 2023. MUTS-based cooperative target stalking for A Multi-USV system. IEEE/CAA J. Autom. Sin. 10, 1582–1592. https://doi.org/10.1109/JAS.2022.106007.

Wang, N., Liu, Y., Gao, Y., 2024. Optimal Trajectory Tracking Control of Unmanned Surface Vehicle Formation Under Unknown Disturbances.

Wu, S., Ye, H., Liu, W., Yang, X., Liu, Z., Zhang, H., 2024. An improved ELOS guidance law for path following of underactuated unmanned surface vehicles. Sensors 24, 5384. https://doi.org/10.3390/s24165384.

Wu, Y., Wang, Y., Feng, Z., Xie, X., 2025. Path following control of uncertain and underactuated autonomous surface vessels. IEEE/CAA J. Autom. Sin. 12 (8), 1730–1732. https://doi.org/10.1109/JAS.2024.124713, 2025.

Yu, H., Wang, X., Zheng, Z., Peng, H., 2025. Formation maintenance strategy for USV fleets based on passive localization under communication constraints. Ocean Eng. 340, 122306. https://doi.org/10.1016/j.oceaneng.2025.122306.

Yu, K., Li, Y., Lv, M., Tong, S., 2024. Distributed optimal formation control of multiple unmanned surface vehicles with stackelberg differential graphical game. IEEE Trans. Arti. Intell. 5, 4058–4073. https://doi.org/10.1109/TAI.2024.3357795.

Zhang, G., Sun, Z., Li, J., Cao, Q., Zhang, W., 2026. Fault-tolerant cooperative formation control for heterogeneous ships: application to the obstacle avoidance maneuvering. IEEE Trans. Autom. Sci. Eng. 23, 2188–2198. https://doi.org/10.1109/TASE.2026.3653021.

Zhang, S., Zhang, Q., Xu, L., Xu, S., Zhang, Y., Hu, Y., 2025. Dynamic sliding mode formation control of unmanned surface vehicles under actuator failure. J. Mar. Sci. Eng. 13, 657. https://doi.org/10.3390/jmse13040657.

Zhou, B., Huang, B., Su, Y., Zhu, C., 2025. Interleaved periodic event-triggered communications-based distributed formation control for cooperative unmanned surface vessels. IEEE Transact. Neural Networks Learn. Syst. 36, 2382–2394. https://doi.org/10.1109/TNNLS.2024.3351218.

Zhou, X., Tian, X., Liu, H., Mai, Q., 2025. Predefined-time cooperative formation control of multiple underactuated unmanned surface vessels with smooth switching topology. https://doi.org/10.1002/rnc.8034.